CONTROLLING QUASI-2D SEPARATION WITH FLOW INJECTION

by

Hunter D. Nowak

A Thesis

Submitted to the Faculty of Purdue University

In Partial Fulfillment of the Requirements for the degree of

Master of Science in Mechanical Engineering

School of Mechanical Engineering

West Lafayette, Indiana

May 2022

THE PURDUE UNIVERSITY GRADUATE SCHOOL

STATEMENT OF COMMITTEE APPROVAL

Dr. Guillermo Paniagua, Chair

School of Mechanical Engineering

Dr. Sally Bane

School of Aeronautics and Astronautics

Dr. John Clark

Air Force Research Laboratory

Dr. Maria Folk

Rolls-Royce Corporation

Dr. Guang Lin

School of Mechanical Engineering

Approved by:

Dr. Nicole L. Key

Dedicated to my parents, who have done nothing but encourage me to pursue my dreams.

ACKNOWLEDGMENTS

I am indebted to Luis Zarate-Sanchez for his efforts in configuring the control system for the successful actuation of flow injection and to Federico Lluesma-Rodriguez for conducting a numerical study which supplemented the work shown below. I would also like to thank Nathaniel Kiefer, Dr. James Braun, Lakshya Bhatnagar, and Michael Butzen for their help in executing the experiments that made this thesis possible. Special thanks to Dr. Iman Rahbari who guided me in my initial endeavors in computational fluid dynamics and provided the analysis which allowed for the proper location of the injection features. Lastly, I would like to thank the countless others from the Purdue Experimental Turbine Aerothermal Lab from whom I have learned so much.

This research is financed by the Air Force Office of Scientific Research, Air Force Material Command, USAF under Award No. FA9550-19-S-0003 Amendment 001.

TABLE OF CONTENTS

LIST OF TABLES

LIST OF FIGURES

NOMENCLATURE

A	Area of test section
A~	Approximate area from Channel Height
A*	Sonic Area
CFD	Computational Fluid Dynamics
FESTO	Pneumatic and electrical automation and control company
ID	Inner Diameter
LPT	Low-Pressure Turbine
M	Mach number
MPS	Miniature Pressure Scanner
OD	Outer Diameter
P	Pressure
PETAL	Purdue Experimental Turbine Aerothermal Laboratory
PIV	Particle Image Velocimetry
PSID	pounds per square inch difference
PR	Total pressure ratio of injection
PT1	PETAL Tunnel 1
PT2	PETAL Tunnel 2
RANS	Reynolds-Averaged Navier-Stokes
Re	Reynolds Number
SB	Separation Bubble
T	Temperature
URANS	Unsteady Reynolds-Averaged Navier-Stokes
VTI	data acquisition system company
1D	one dimensional
2D	two dimensional
3D	three dimensional

SUBSCRIPTS

0	Total
Crest	at the crest
S	Static
Local	at a given x-coordinate
Exit	at last wall pressure tap

ABSTRACT

Highly loaded aerodynamic devices for propulsion and power generation are emerging to increase power output in a more compact machine are emerging. These devices can experience increased losses due to separation, as in the low-pressure turbine, which arise due to the operation at conditions that increases the adverse pressure gradients ore decrease the Reynolds number of the flow through the device. Therefore, flow control strategies become appealing to reduce losses at these conditions. This work aims to validate flow injection as an effective flow control strategy in the transonic regime.

A test facility which was used to study boundary layer separation in a quasi-2d test article was modified to include flow injection and conditions were modified so that the facility was operated in the transonic regime. Valves were chosen which could achieve a wide range of excitation frequencies and the flow control ports were designed to accommodate their nominal flow rate. A preliminary test matrix was built while considering the limitations of the test facility.

A numerical study was conducted to identify flow structures of interest and determine a preliminary understanding of the test article. The flow control was then added to the numerical study to guide the experimental set points for injected flow. The response of the flow to continuous slot blowing was characterized, and a 3D simulation with discrete injection ports was done to ensure the set-points determined from the 2D study were viable for discrete injection.

Blow-down experiments were then conducted to study the behavior of bulk separation in a transonic regime for a quasi-2D geometry. Once behavior of the separation was understood, steady injection and then pulsated injection were applied in attempts to mitigate the separation. Steady injection was utilized to find the required pressure of injection relative to the total pressure at the inlet of the test article, while the pulsated injection served to identify a frequency at which the time averaged mitigation of separation was greatest.

The experiments show that both steady and pulsated flow injection are viable techniques in flow control. It is also shown that pulsation does not allow for a lower pressure injection, but instead allows for the same effect with a lower mass flow requirement. Two-dimensional computational simulations are shown to be effective in determining injection frequencies but not the extent of separation or required injection pressures.

1. INTRODUCTION

New classes and generations of turbine airfoils that experience losses due to separated flows at depressed Reynolds numbers are emerging. As such, active flow control becomes a desired technology to mitigate these losses in the separated portion of operation. This section of the thesis provides a literature survey on the current state of the art of flow injection in internal flows, defines the objectives of the research, outlines the methodology used to achieve the objectives, and defines the architecture of the thesis itself.

1.1 State of the Art

Propulsion and power generation systems which utilize devices that push the bounds of operability when compared to current state-of-the-art systems. Prime examples of this, are the low-pressure turbine (LPT) blades designed and studied by Praisner et al. (2013) and Schmitz et al. (2016), which experienced increased losses at depressed Reynolds numbers increased the loading. The airfoils studied by Praisner et al. (2013) have an exit Mach number of 0.65 and experience degraded performance at low Reynolds numbers due to the presence of flow separation. Passive and active flow control strategies to extend the performance of aerothermal devices have been of significant interest in recent decades. Passive flow control techniques that mitigate separation are accompanied by penalties at the design condition, making them less palatable, as discussed by Volino (2003). Active control techniques may allow for little impact to performance while at nominal operation. As designers increase the loading of turbine airfoils, Mach numbers throughout the turbine passage will also increase, necessitating the study of flow separation and control in transonic regimes.

Separated flows are often studied by imposing a pressure gradient on a flat airfoil with a contoured test section, as done by Coull and Hodson (2011). Similarly, wall-mounted humps are used to consider the effects of local curvature, as in Saavedra and Paniagua (2021), and to characterize flow control via steady injection, as in Luedke et al. (2005). Wall-mounted humps allow for the investigation of separated flows as Reynolds and Mach number are allowed to change. Several studies, such as that of Seifert and Pack (2002), use numerical tools to model separation for wall-mounted humps and the introduction of flow injection as a method of flow control. The

most common geometry studied is the 2D NASA wall-mounted hump separated flow validation case, as done in You et al. (2006), Morgan et al. (2007), Iyer and Malik (2016), and others. This geometry, although useful in studying separation and its response to flow injection, is primarily used as a numerical tool in the validation of computational fluid dynamics (CFD) solvers at low Mach numbers and relatively high Reynolds numbers.

The control of separation by periodic excitation for external flows has been comprehensively summarized by Greenblatt and Wygnaski (2000). Pack and Seifert (1999) studied periodic jet excitation for the enhanced performance of diffusers and greater control of the direction of the exiting flow. Similarly, the wall-mounted hump studied in Luedke et al. (2005) vented immediately into ambient conditions. The lack of ducting downstream of the wall-mounted hump may artificially alter the extent of the separation caused by the shape and pressure gradient imposed by the geometry of the test section. In fully internal, wall-mounted humps, Saavedra and Paniagua (2021) inspect the effect of Reynolds on flow detachment and the effects of suddenly starting flow into the test article. It was found that suddenly imposed inlet conditions, as opposed to ramping to the target condition, allowed flow to adhere to the surface of the wall-mounted hump. Due to this greater ability to remain attached in transient conditions, pulsated injection should be an avenue of development as the transient effects may enhance the impact of flow injection. In Saavedra (2018), the effects of adding a sinusoidal pressure signal near the point of separation was studied, and numerically shown be a viable method to mitigate separation.

Additional strategies such as dielectric barrier discharge (DBD) actuators have been demonstrated for these low Mach numbers, as shown by Opaits et al. (2008), Leonov et al. (2011), Pescini et al. (2017), and Martinez et al (2017). All of these studies were conducted with flow velocities well below 100 m/s, due to the lack of additional velocity induced by DBD devices. For supersonic flows, even more alternative methods of flow control are discussed. Cybyk et al. (2006, January) show the effective ness of synthetic jet actuation, and Kandala and Candler (2004) conducted a numerical study on the effectiveness of energy deposition.

All the aforementioned studies regarding experimental implementations of flow injection to internal passages were conducted with Mach numbers below 0.25. Many efforts were made in demonstrating steady and pulsated flow injection in this low inlet Mach regime for various geometries, however many of the studies were closer to diffusers than fully internal flows experiencing separation. For internal flows in the low supersonic regime alternate flow control

strategies were considered, however flow injection in the transonic regime has not been demonstrated. At low Reynolds numbers the ratio of momentum effects to viscous effects may be the same, but at higher speed the main flow has more energy. Similarly, at higher speeds the effects of local curvature could be more dominant, as the flow may move rapidly enough to separate due to curvature alone. Therefore, the response of the boundary layer may be different at higher Mach numbers when compared to prior, low-speed studies. The emerging classes of transonic low-pressure turbines which experience separation at low Reynolds, necessitate the demonstration and development of flow injection so that the performance benefits of increased loading can be realized throughout the operating regime of the LPT. The strength of the wakes in these devices could allow for the development of the separation past the trailing edge of the turbine blade itself, requiring a test case which has continuous walls well past the separation and does not immediately diverge to ambient conditions.

1.2 Research Objectives

This thesis sets out to demonstrate flow injection as an effective method of flow control for internal flows in the transonic regime. Prior works, discussed in section 1.1, use alternative methods of control in transonic regimes or sonic regimes. Flow injection may be a promising technique for control in applications where air can be supplied with relative ease.

1.3 Research Methodology

The objective of this thesis was completed in three phases: the design of the 3D wall-mounted hump and test sequence, the computational assessment of the test matrix and the response to flow control, and experimentation using a blowdown wind tunnel.

The original design of the 3D hump is taken from the open-source geometry provided by Saavedra and Paniagua (2021). The geometry was modified to incorporate a flow injection system capable of actuation frequencies between 0 and 1 kHz. The design of the system included the sizing of the injection ports to adequately pass the mass flow provided by the actuation valves chosen. Wall pressure taps were used to assess the time-averaged separation to verify that the geometry reproduced the well-studied behavior documented by previous researchers without any flow control. Similarly, high-speed schlieren imagery was used to characterize the time resolved flow

field. The Reynolds numbers where the airfoils studied by Praisner et al. (2013) begin to experience increased losses were used to build an initial starting point for the experimental domain. The area of the inlet and throat of the test article were used to calculate an inlet Mach number that would lead to near sonic conditions at the throat of the test article.

Once the approximate inlet Mach number was known and appropriate boundary were identified, a computational study was conducted to fully define inlet conditions for an experimental campaign. The centerline of the test article, including flow injection ports, is taken to perform 2D CFD (computational fluid dynamics) in Ansys Fluent. The combination of Reynolds and Mach numbers identified earlier were computationally explored to ensure the existence of a large-scale separation. The base flows were used to numerically explore various flow injection quantities used to build a full experimental matrix. Unsteady simulations of the lowest realizable pressure for the chosen valves were conducted with various forcing frequencies. A 3D domain was built, and a mesh was generated HEXPRESS to assess the injection performance in 3D. The 3D domain was used to assess separation compared to the 2D case and a singular injection pressure greater than was effective in 2D was evaluated. A full experimental matrix was built to show the effect of various flow control quantities to the base flows defined by the experimental matrix.

The experimental matrix was then applied to the test article in the blow-down facility. The behavior of the separation in absence of flow control was assessed with wall pressure taps. Schlieren imaging of the crest of the hump to observe potential shock structures on start-up. Steady injection was applied, and the response of the separated region was assessed with the same techniques. Finally, unsteady flow injection was applied and the response of the separated region was observed.

The data collected from the experiments was used to identify effective frequencies and injection manifold quantities to guide future applications of flow control in transonic regimes.

1.4 Thesis Layout

This document details the work done to experimentally demonstrate flow injection as a viable strategy for application to transonic internal flows. The introduction, chapter one, laid the ground work in establishing the state-of-the-art prior works, identified the lapse in literature and clearly defined the objectives of this thesis and the methodology to achieve said objectives. Chapter two details the design process of the test article, the design of the experiments and

describes how the facility is operated and how each measurement technique is applied to identify quantities of interest. Chapter three details the experimental findings in several stages. Initially, the base flow fields and the structure of a blow-down are shown, followed by the response to steady and unsteady flow injection. The conclusion serves to present the implications of the experimental findings, provide recommendations for further improvements, and a direction to head for future endeavors.

2. EXPERIMENTAL RESEARCH METHOD

The geometry of Saavedra and Paniagua (2021) exhibited separation at a depressed inlet Mach number and was chosen to be the focus in the application of flow control. Global stability solvers use numerical solutions to find different eigenmodes of the flow field and ultimately determine where a flow field is most sensitive to excitation. Wang et al. (2021) used a global stability solver and to locate a flow control feature and determine the most suitable angle for injection. The geometry of Saavedra and Paniagua (2021) was taken along with the identified axial location based on the results of the global stability solver detailed in Rahbari and Paniagua (2020) as an ideal test case to extend understanding into the transonic regime.

The test article was modified to enable the use of flow injection. A high frequency solenoid valve was chosen such that a large range of suitable frequencies of injection were possible at a sufficient flow rate. Flow control features in the form of slots and supply tubes were chosen such that they interface properly with both the chosen valves and the available space in the test article. Wall pressure taps were added just off the centerline and inserts were designed for higher frequency measurements to be used in future studies.

A series of Reynolds numbers, based on the regime where the airfoils studied by Praisner et al. (2013) were chosen as conditions of interest. The areas of the throat of the test article and the inlet of the test article were used to identify inlet Mach numbers that would lead to near sonic conditions at the throat. Total inlet quantities and static exit pressure were then found to impose the different Reynolds and Mach numbers. The center line of the 3D test article was used to perform CFD simulations to assess the preliminary experimental matrix. For each Reynolds number, a set of total pressures of injected flow were assessed. For the highest Reynolds case, a series of frequencies of flow injection were investigated for the highest total pressure of injection.

A test sequence was designed such that the range of Reynolds and Mach numbers that encompass the 2D numerical quantities were possible to attain with the use of the PETAL blowdown facility, detailed in Saavedra and Paniagua (2021).

2.1 Test Article Design

Based on the studies presented by Saavedra and Paniagua (2021) and Saavedra (2018) forcing frequencies between 50 and 250 Hz were deemed to be optimal in flow injection for the mitigation of bulk separation in the channel with a low inlet Mach number. A series of valves were chosen, such that frequencies well above the range identified by Saavedra (2018) were attainable. The end result is that a valve from FESTO capable of actuating at 1000 Hz and delivering a nominal flow rate of 100 l/min was chosen. The FESTO valves are a solenoid actuated poppet valve, which results in a pressure signal that is a square wave with some added delay in rise and fall time, fig 2.1.

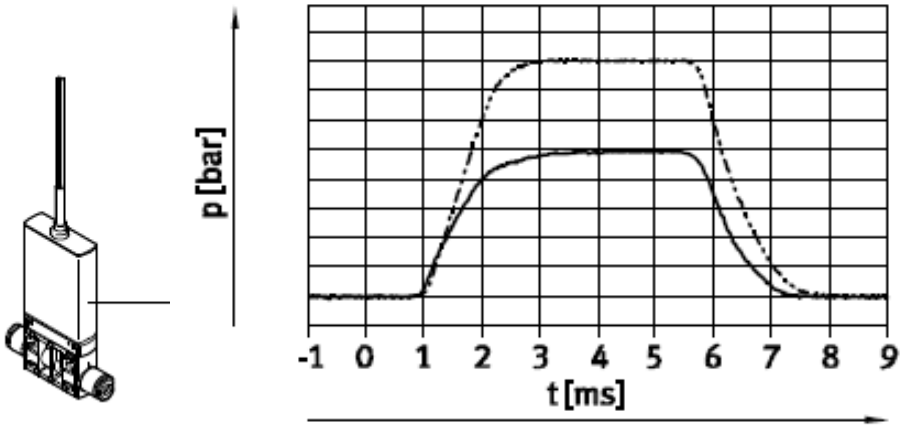

Figure 2.1 FESTO MHJ-10-S-0,35-QS-1/4-MF-U (valve model) and associated pressure signal [FESTO (2019)]

Using the inlet conditions of the studies presented by Saavedra and Paniagua (2021), the solver detailed by Rahbari and Paniagua (2020) identified the axial location at which the flow field was most sensitive to excitation. A study by Wang et al. (2021) showed that air used for the purpose of flow injection was most effective when introduced 10 degrees above the tangent of the surface of a wall-mounted hump. The angle of injection chosen is that which was recommended by Wang et al. (2021). Taking the nominal flow rate of the valve, a slot was designed such that the air to be used for flow control would choke the flow control port. The end result was a 1 mm tall, and 2.7 mm wide slot with 0.5 mm radii, figure 2.2.

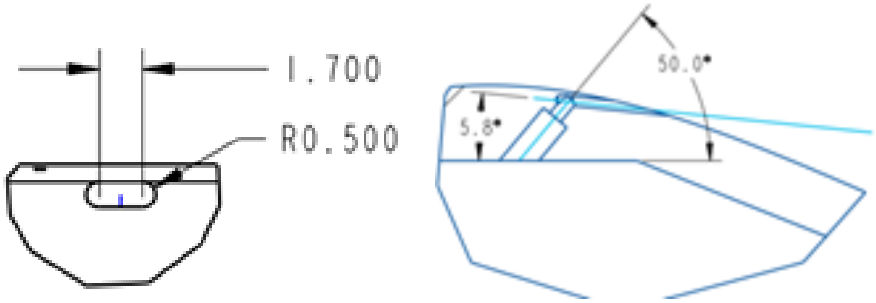

Figure 2.2 Drawing details of flow injection slot (dimensions in mm)

With the target location and geometry of the slot known, the full supply path of the valves was designed. The tubing upstream of the injection slot was sized so that the area of the tubing was larger than the area of the injection slot. This resulted in a supply path from the valve stepping from 1/4” OD (outer diameter), 1/8” ID (inner diameter) tubing to 3mm OD, 1.8 mm ID tubing which then directly supplied the injection slot. A region of the original 3D hump, was made hollow so there was room to add the features necessary to facilitate flow control. A series of fifteen slots centered along the central axis of the test article were created so the tubing could be installed using epoxy. These ports were each 1/4” apart from each other.

The experimental study of Saavedra and Paniagua (2021), showed that for the subsonic inlet conditions explored, pressure measurements on the central 10% of the span exhibit no spanwise dependence. It was assumed the same would be true for the transonic regime, which resulted in a single line of pressure taps 1/8” off centerline, or directly in-between the central flow control slot and one of its neighboring slots. There is a pressure tap directly on the crest of the test article, after which each pressure tap is 10 mm arclength farther downstream. Pressure taps along this line upstream of the crest start 1.5 inches downstream of the leading edge and have a spacing of 1.25 inches. A row of 3 pressure taps 25.4 mm from the leading edge of the test article were used to check the spanwise pressure deviations at the inlet of the test article. They are centered on 50% span and are spaced 3/4” from each other. A total of 44 pressure taps were used to evaluate wall pressures along the topology of the wall mounted hump. The surface of the wall-mounted hump has a surface finish of 16 micro-inches, which is representative of a smooth internal ducting, but small relative to the curvature when compared to an airfoil. The locations of the injection slots, pressure taps can be seen in figure 2.3 and the final installation of the test article can be seen in figure 2.4.

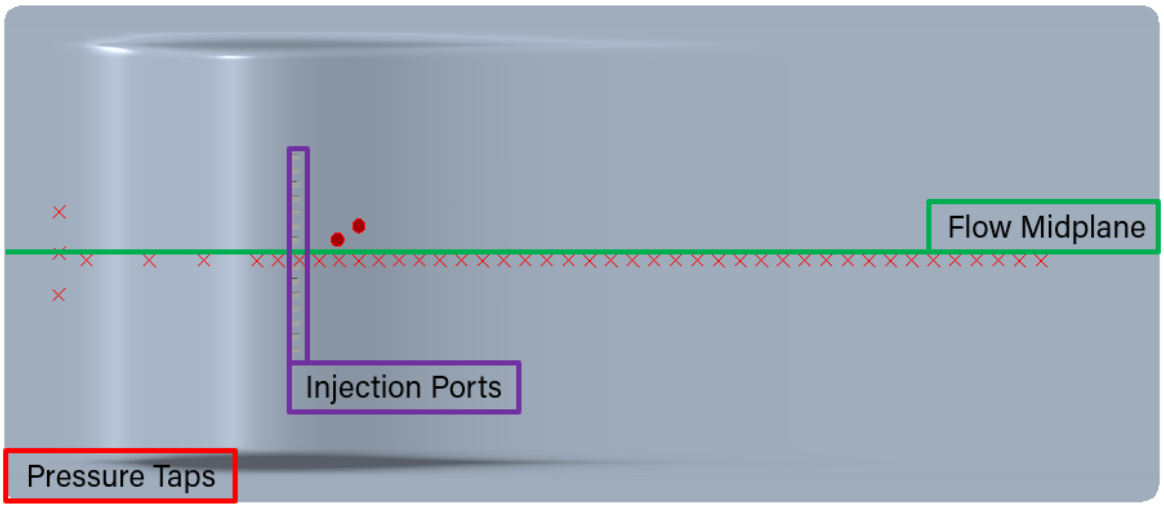

Figure 2.3 Wall pressure tap and injection port location

Figure 2.4 Test article installed in PT1

2.2 Measurement Techniques

To quantify the inlet conditions during the experimental campaign, a pressure tap, total pressure probe and total temperature probe were used. The pressure tap was located in the same axial position as both the total pressure and temperature probes. The total pressure probe was a

shielded or Kiel pitot probe and the total temperature probe was an unshielded k-type thermocouple. These three measuring devices allowed for the assessment of inlet Mach and Reynolds numbers throughout the duration of each individual the blow down. The location of these measurement devices is shown in figure 2.5.

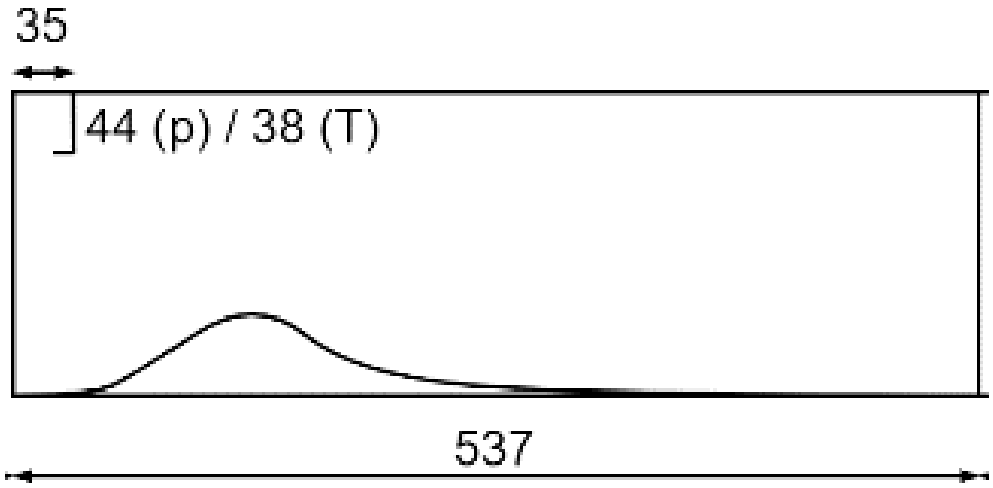

Figure 2.5 Schematic location of total quantity measurements and inlet static pressure measurement. Numbers represent depth, in mm, of insertion for each probe

Wall pressures of the wall-mounted hump were assessed using the series of pressure taps previously described. The pressure taps were coupled to a 50 psid ScaniValve MPS pressure transducer capable of sampling up to 800 Hz. The MPS was used to acquire the other relevant pressures, the previously mentioned inlet total and static pressures and the total pressure in the manifold used for the injection air supply. The only time discrepancy in pressure measurements was from the varying lengths of tubing due to the distance between the measurement location and the MPS. To mitigate the timing discrepancy, all pressure taps along the wall-mounted hump were cut to the same length, about 36 in., while the pneumatic lines for inlet and manifold pressures were significantly longer.

The design of the wind tunnel allowed for optical measurement techniques. For this study a linear schlieren set up was used to determine start up behavior along with the flow structures of the experimental blow downs. Different frame rates were chosen depending on the time scale of features to be resolved. A z-type schlieren set up was used for the investigation of pulsated flow injection. As for the linear schlieren set-up, results shown will indicate the frame rate and denote the set-up. The set-ups and regions of observation can be found in figure 2.6.

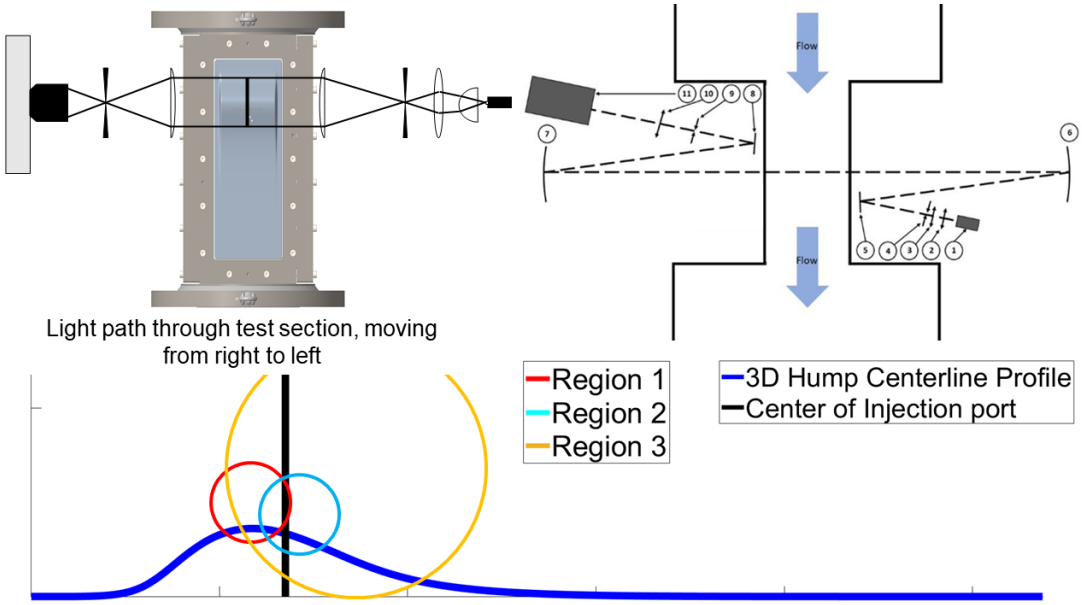

Figure 2.6. Schematic Representation of approximate schlieren imaging set-ups and regions [Kiefer (2022)]

2.3 Test Sequence

The PETAL facility consists of two blow-down wind tunnels which are isolated from the high-pressure system by fast-acting butterfly valves and from the low-pressure system by variable area sonic valves or a steel plate which is installed when the test article is not in use. Each test section is capable of achieving sub atmospheric pressures and a range of total temperatures dependent upon the heat output of a large gas heat exchanger and the mass flow desired for a blowdown. The experimental work presented in this thesis utilized the linear test section, PT1, while keeping PT2 entirely isolated from the imposed pressures in the system. To operate the facility, exit pressure must be established in the vacuum tank, inlet mass flow and temperature must be established through the purge line. Then the fast-acting valves must open to allow flow to enter the test section, and the purge valve must close so the established mass flow does not bleed through the purge line. This order is then reversed at the end of the blow down to re-establish flow through the purge line, stopping flow through the test article. The sonic valve shown in figure 2.7 which usually isolates the test section from downstream pressure variations is not present. This means the static exit pressure increased throughout the duration of each blow-down. Each blow-

down had a duration limited to 11 seconds. A rise in vacuum to levels higher than absolutely necessary increased the total time required for each experimental campaign.

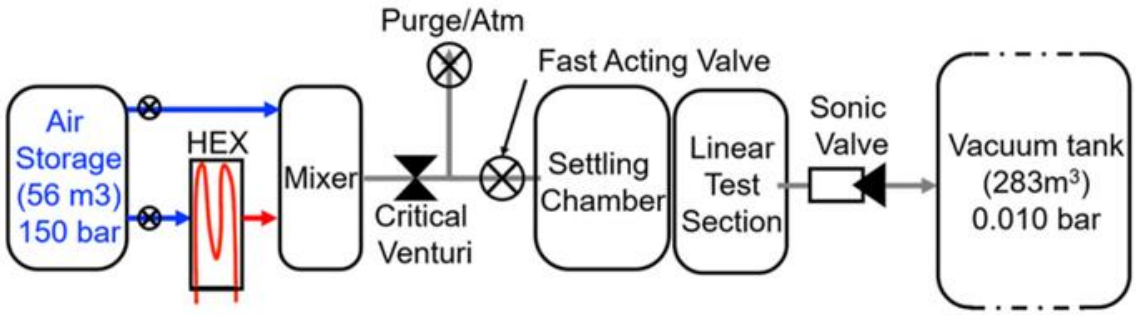

Figure 2.7. PETAL facility schematic [Saavedra (2021)]

To ensure a transonic regime of flow over the crest of the wall-mounted hump isentropic flow relationships were used. The approximate area of the wind tunnel was found by subtracting the crest height from the height of the channel of the wind tunnel. This wind tunnel area was used to determine an approximation for the inlet Mach number at which the flow at the throat of the channel would be sonic. The real area of the wind tunnel at the crest was extracted from the CAD model of the test article, from which the approximation could be compared to determine the potential decrease in Mach number caused by the grooves on the geometry from Saavedra and Paniagua (2021).

The area of the test section at the crest was taken as the sonic area for use in the 1D isentropic flow equations, while the approximate area neglected the added area from the grooves near the end walls. The inlet area divided by the approximate crest area yielded an A/A* of 1.27, which in turn yielded a Mach number of 0.54 on the subsonic branch of solutions. The area of the real throat was 5% larger than the throat calculated neglecting the grooves. If an inlet Mach number of 0.5 is imposed as the upper limit, the area at the crest is 10% larger than the sonic area of the flow. This margin in area was added to mitigate the risk of creating a supersonic passage during experiments.

When evaluating the imposed Mach number of 0.5 using A/A* and the real area of the throat of the test article, the Mach number at the crest was found to be 0.69. When using the channel heights at the inlet and at the crest (neglecting the grooves) the Mach number at the crest was found to be 0.76. As it was shown by Saavedra and Paniagua (2021) that the channel is pseudo 2D at the centerline of the test article, it was assumed the elevated Mach number found using channel heights

would be more representative of what would be observed and sufficiently transonic to assess the behavior of flow separation.

A set of Reynolds numbers were chosen such that a similar flow regime to the region at which the airfoils of Praisner et al. (2013) experienced increased losses, and prior studies by Saavedra (2018) and Saavedra and Paniagua (2021). They were used to determine inlet conditions and requisite vacuum levels in the downstream tank. The Reynolds numbers per chosen ranged between two million per meter to 3.5 million per meter in increments of 500 thousand. Prior experience within PETAL suggested that due to the short duration and relatively low mass flows for similar Mach and Reynolds numbers, total temperatures rarely reached above 410K at the inlet of the test section, therefore, total temperature targets were set to 405K. The limit of 410K due to potential losses in heat as a result of cold upstream piping due to the short duration expected of each blowdown.

The nominal inlet conditions and required vacuum levels were found by iteratively solving the following system of equations (using the appropriate Sutherland's law coefficients) for a desired total pressure with an inlet Mach number of 0.5 and the previously mentioned total temperature limit. This process was repeated for an inlet Mach number of 0.4, while ensuring the mass flow was the identical to that found for an inlet Mach number of 0.5. The total and static pressures increase, while the mass flow and total temperature remain constant. The Reynolds number drops slightly when the Mach number is allowed to drop. This matches the expected effects of holding the upstream facility constant while allowing the downstream vacuum tank to fill over time.

$$Reynolds\ /m = \frac{Pu}{RT\mu}$$

$$T = T_0 * \left(1 + \frac{\gamma - 1}{2} * M^2\right)^{-1}$$

$$P = P_0 * \left(1 + \frac{\gamma - 1}{2} * M^2\right)^{\left(\frac{-\gamma}{\gamma - 1}\right)}$$

$$u = M * \sqrt{\gamma R T}$$

$$\mu = \mu_{ref} \left(\frac{T}{T_{ref}}\right)^{3/2} \frac{T_{ref} + S}{T + S}$$

The effect of the varying downstream pressure was approximated using a combination of a 1D isentropic flow relations and existing MATLAB scripts which predict the pressure of the downstream vacuum tank using the ideal gas law. The scripts took a minimum vacuum pressure and calculate the mass of the air within the volume of vacuum tank. Then for an array of times, mass was incrementally added to the vacuum tank at the rate at which it flows through the test article, and recalculated the pressure of the air in the vacuum tank. The temperature was assumed to change based on the mass fractions of the added air from the test article and the stagnant air in the tank. By using nominal total quantities and exit static pressure and assuming the mass flow will remain constant, the time between the inlet Mach 0.5 and inlet Mach 0.4 cases was found as the time between the two instances where the vacuum tank had a pressure which matched the static pressure for each Mach number. The set points can be calculated again for a lower total temperature to remove the requirement of the heater. The conditions targeted are summarized in table 2.1 below.

Table 2.1. Experimental target conditions

Exp #	Re	Mach	T_0 [K]	$\dot{m}$ [kg/s]	$P_{s,exit}$ [Bar]	Δt [s]
1	2.00e6 /m	0.5	405	1.7	0.243	-
	1.98e6/m	0.4	405	1.7	0.306	8.5
2	2.50e6/m	0.5	405	2.1	0.304	-
	2.47e6/m	0.4	405	2.1	0.383	9.5
3	3.00e6/m	0.5	405	2.5	0.365	-
	2.97e6/m	0.4	405	2.5	0.460	8.7
4	3.50e6/m	0.5	405	3.0	0.425	-
	3.46e6/m	0.4	405	3.0	0.536	8.0

Since the duration of the test between two potential inlet Mach numbers are known for four Reynolds numbers, the facility operation can be designed in a manner to facilitate the maximum amount of relevant data. The operation was as follows: vacuum was pulled after ensuring total control of the facility. In the case using hot air, mass flow and temperature targets were established through a bypass line (the purge line). For the use of cold air, only mass flow was established as no heater was used. Once flow conditions are stable, an automated sequence that opens the test section to the supply line, and closes the valve to the bypass was run. After 11 seconds the valves

were actuated in opposite order. If schlieren imagery was to be taken for a particular blow-down, the triggering of the high-speed camera was built into the automated sequence for consistent results. The experiment was repeated or the vacuum level was adjusted to hit a different target condition. The operation with implemented flow control looked the same, with the additional steps of setting the pressure in a supply manifold and frequency of operation for the injection slots prior to ramping up flow through the bypass and shutting off the FESTO valves and reducing manifold pressure after flow through bypass has stopped. The set points for the flow control were informed by a brief numerical study and some preliminary experiments and are summarized in the appendix.

2.4 Computational Assessment of Experimental Matrix

The center line of the 3D test article was used to create a 2D domain to assess the matrix proposed in section 2.3. The inlet Mach 0.5 conditions in table 2.1 are used as the boundary conditions for the numerical work. The mesh of the 2D domain was generated by breaking the domain into the groups shown in figure 2.8 and meshing each block using the ANSYS mesh tools in ANSYS workbench.

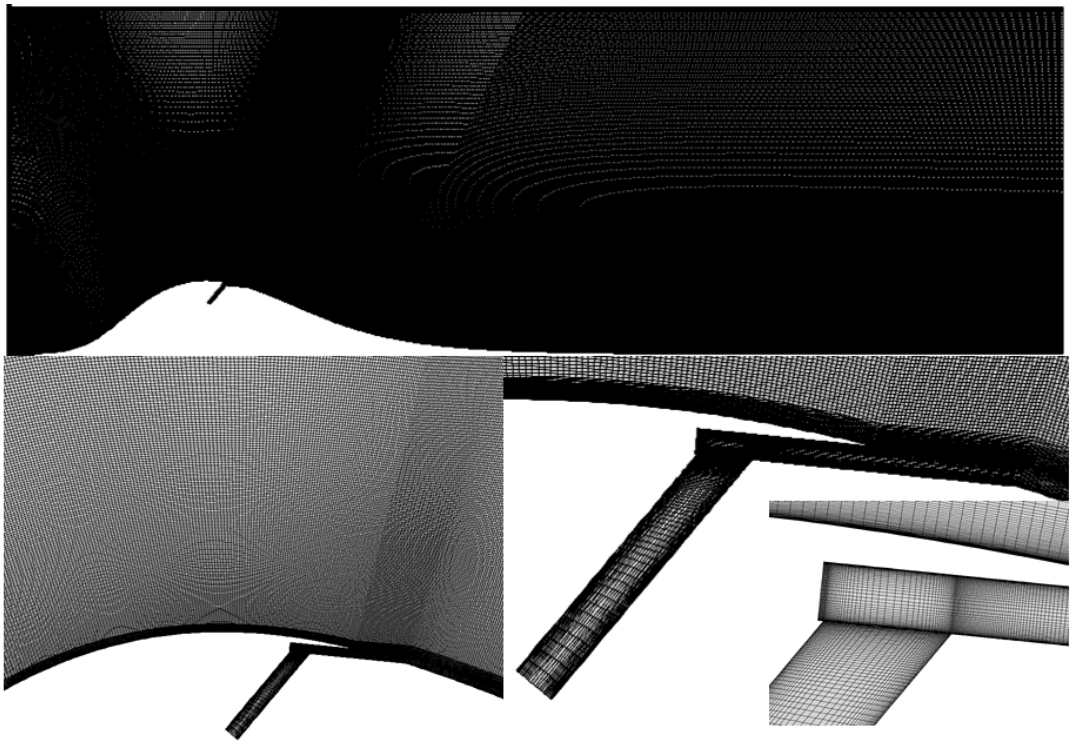

Figure 2.8. Mesh Topology of 2D computational Domain

For all results of the 2D RANS (Reynolds-Averaged Navier-Stokes) simulations presented, the following solver settings for ANSYS Fluent were used. A pressure-based solver with second-order (upwind when available) spatial discretization was used. Energy equations were included and the k-ω SST turbulence model with low Reynolds correction and compressibility effects was used. The Courant number was 200. Pressure-velocity coupling was turned on with relaxation factors of 0.5 for both momentum and pressure.

The three million Reynolds /m case was used to conduct a mesh sensitivity study according to the guidelines set by Celik et al. (2008). Area weighted total pressure losses from inlet to outlet, viscous drag along the bottom wall, outlet mass flow, and separation length were used as the quantities of interest for the convergence study. The difference in quantities of interest between each mesh size are taken, and error between the three meshes is extrapolated. The extrapolated error is used to determine the fine grid convergence index. Four meshes of increasing node density were used to conduct the study, the results of the coarsest three are shown below. A density-based solver with implicit formulation and ROE-FDS flux was then run on the medium mesh from the grid sensitivity study, to determine the difference in the solver formulations.

Table 2.2. Grid sensitivity results following the method of Celik et al.

Mesh ID	Nodes	r	Mean e_a	Mean GCI
Coarse	219996	1.25	11.27%	0.80%
Mid	347564			
Fine	488831	1.19	0.62%	0.11%

The medium mesh was chosen for the following numerical study as the mean extrapolated error between the medium and fine meshes was less than 1% and it saved significantly on computational time. The density-based solver was not used due to changes in the results depending upon when the simulation was stopped. This implied an unsteady simulation was required which

would have significantly increased computational demand. Wall quantities of the simulations are shown in figure 2.9.

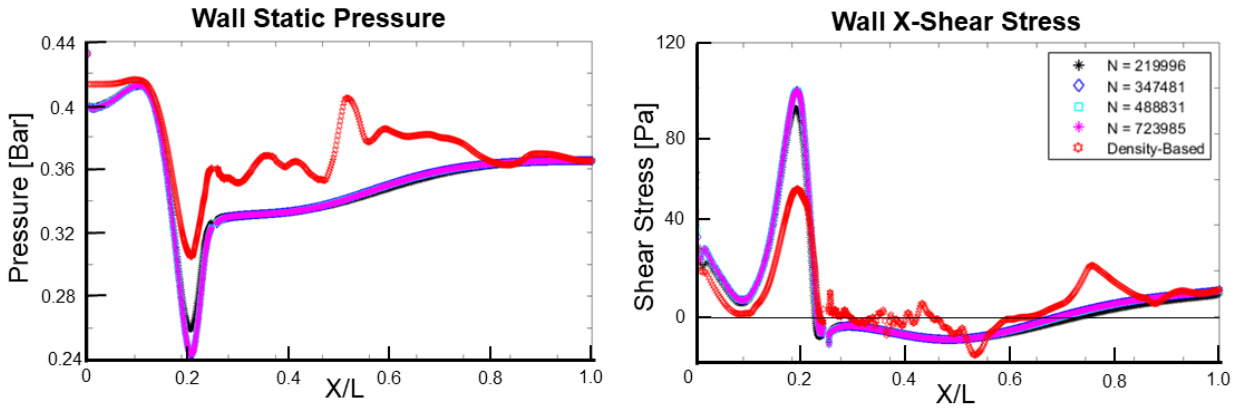

Figure 2.9. Wall quantities for four grids and 2nd coarsest mesh with density-based solver

The different Reynolds numbers were then simulated with the settings described using the pressure-based solver. The results showed in the range of Reynolds numbers analyzed, the length of separation is relatively insensitive to Reynolds number (fig 2.10 left below). Figure 2.10 shows that isentropic Mach number along the bottom wall (figure 2.10 left) can be used as a predictor of separation length, which is shown distinctly with wall shear stress (fig 2.10 right). The change in slope of isentropic Mach number towards horizontal at an X/L near 0.25 is indicative of the onset of separation. This is mirrored in wall shear stress in the x-direction as the value becomes negative, indicating flow towards the inlet of the domain. The reattachment point is less clear in the isentropic Mach number distribution, but occurs after isentropic Mach number has decreased and returned towards a stable value close to that of the exit (near X/L of 0.7). This is mirrored in the wall shear stress when the value becomes positive, indicating flow is moving towards the exit. Results show the curvature of the wall mounted hump increases the local Mach number to approximately 0.98, which is significantly higher than the 1D approximation found when developing the inlet conditions, but are closer to peak Mach numbers which may be seen in transonic airfoils.

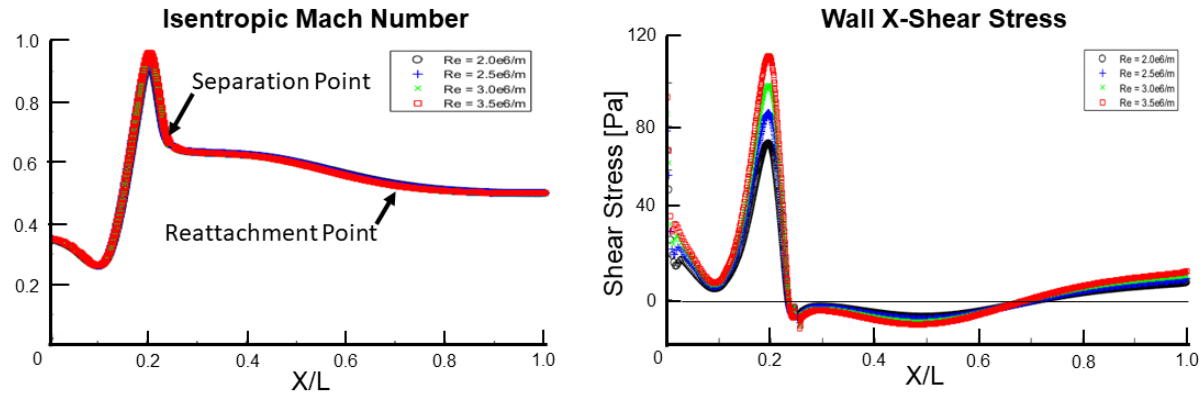

Figure 2.10. Isentropic Mach number and wall x-shear stress for varying Reynolds /m

Since solvers can fail to accurately predict separated regimes and their associated pressure losses, as shown by Schmitz et al (2016), the results were used to predict regimes where separation might occur. The numerical study was extended to analyze steady flow injection by adding a total pressure inlet for the supply tubing. The 2D domain ends approximately five diameters of the smallest supply tubing before the elbow shown in figure 2.8. Total pressures between 97.1% and 208.1% of the total pressure of the main channel were imposed as total pressure inlets at the flow control port. The pressures were incremented by either 5 or 10 kPa and the total temperature was set to 290 K, or approximately ambient conditions. The response of the bulk separation to the different steady flow injection was assessed by comparing isentropic Mach number and wall shear stress to the base flows at the same Reynolds number. Total pressure ratio was chosen to characterize the injection as is directly measurable.

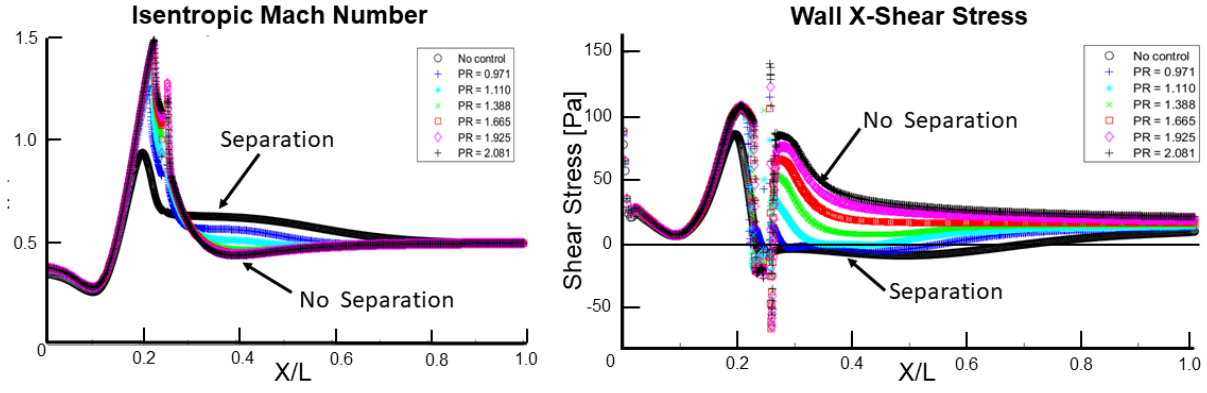

Figure 2.11. RE 2.5 million /m Isentropic Mach and Shear stress response to steady injection

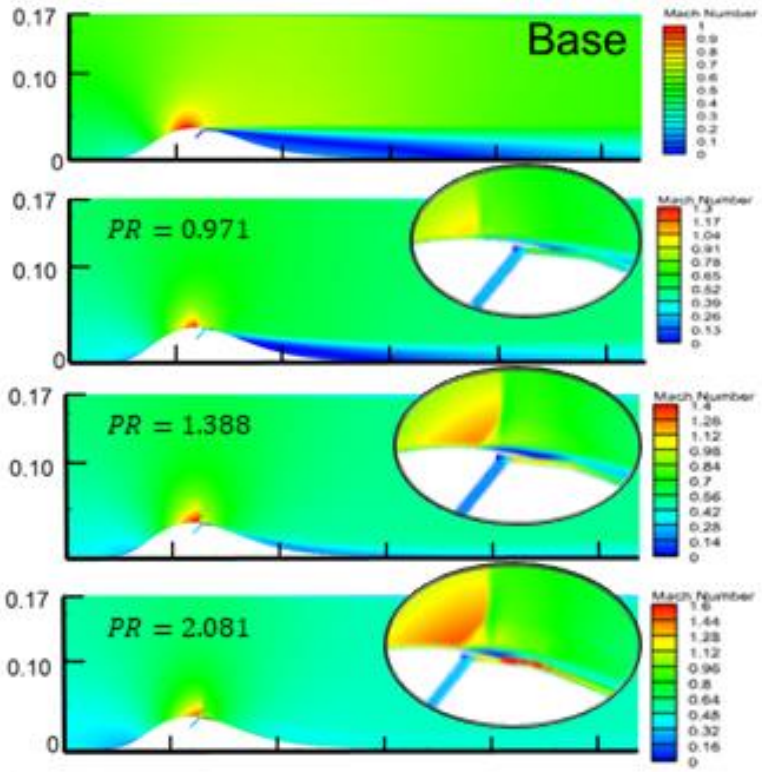

Figure 2.12. Re 3.5 million /m Mach contours with varying injection pressures

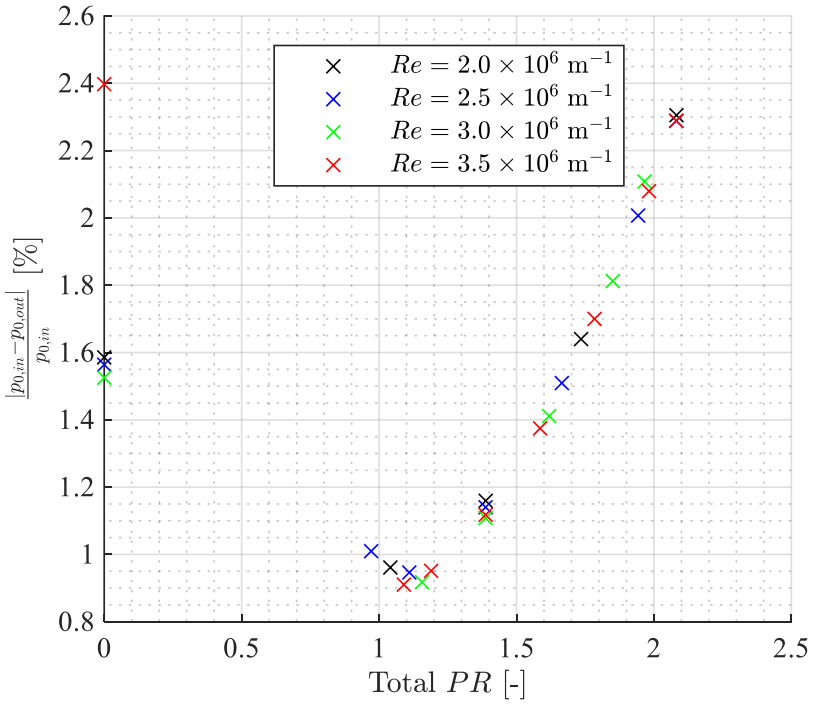

Figure 2.13. Total Pressure Losses as a Function of total Pressure Ratio

Total pressure losses were calculated according to the following equation:

$$Total\ Pressure\ Loss = \frac{\left|P_{0,in} - P_{0,out}\right|}{P_{0,in}} * 100\ \%$$

Where $P_{0,out}$ was the mass weighted average of total pressure at the exit of the domain, extracted from Fluent and $P_{0,in}$ was calculated as follows:

$$P_{0,in} = \frac{P_{0,in} * \dot{m}_{inlet} + P_{0,control} * \dot{m}_{control}}{\dot{m}_{inlet} + \dot{m}_{control}}$$

Figure 2.13 shows that total pressure losses begin to increase as the total pressure ratio (PR) increases past approximately 1.18. As the pressure ratio increases, a shock appears near the crest and moves downstream and increases in strength with increasing total pressure ratios, seen in figure 2.12. The increased strength of the shock combined with added pressure that is no longer contributing to the suppression of the separated region lead to the increase in mass-weighted total pressure losses from inlets to outlet. Figure 2.11 shows, of the pressure ratios investigated, a total pressure ratio of 1.110 (for Reynolds = 2.5 million /m) is the minimum required to remove a large recirculation. The isentropic Mach number along the bottom wall for the same condition shows a small region of horizontal slope in the isentropic Mach number showing the presence of a separated region. It can be seen however, that at total pressure ratios at or greater than 1.110 the total pressure losses increase. The increased pressure of the injected flow is no longer necessary to suppress separation or pressure loses.

Figure 2.14 shows the growing prevalence of the total pressure decrease due to the increased strength of the shock induced by flow injection. The total pressure loss of the flow without control is near 1.6%, for the PR = 0.971 case the total pressure losses are just over 1%, while the total pressure loss of the PR = 2.081 case is just over 2.3%. The shock contributes to a local decrease in total pressure of around 3 kPa, which is not present for low total pressure ratios. This demonstrates the impact of the shock structure that forms and emphasizes the lowest pressure of injection that suppresses separation should be targeted for engineering applications. The highest pressure ratio investigated for the 3.5 million Reynolds /m case resulted in the injection of 1.75% of the mass flow at the inlet of the test article through the modeled slot.

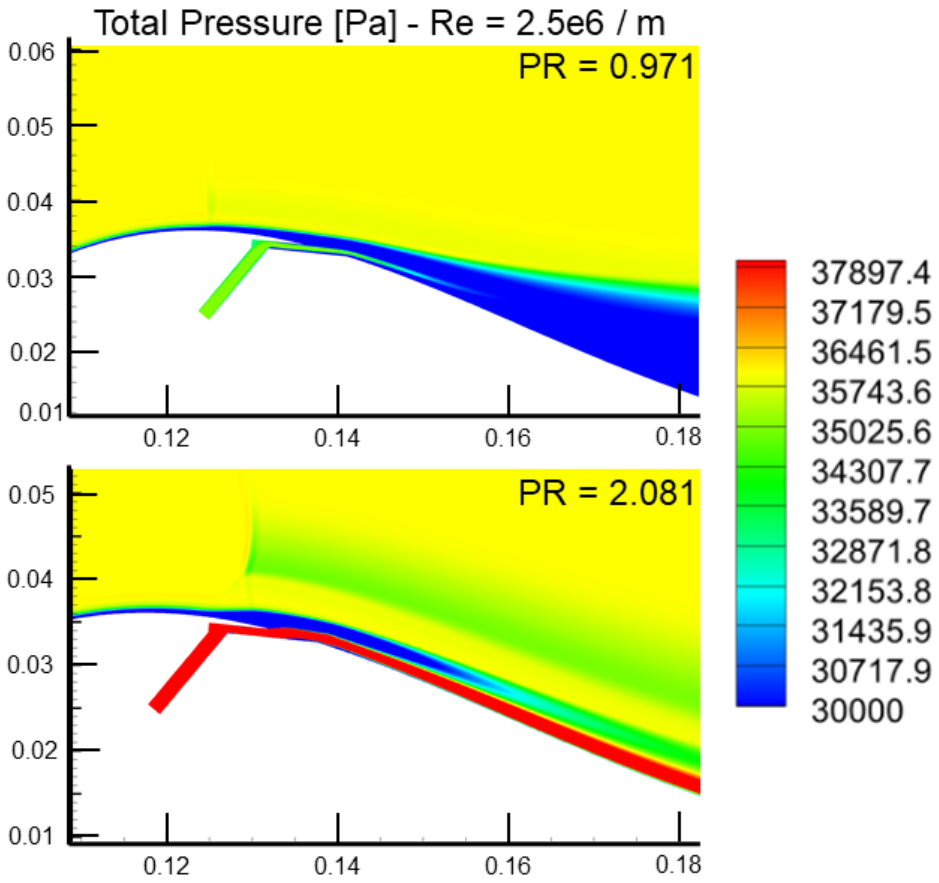

Figure 2.14. Total pressure contours for two selected total pressure ratios at 3.5 million Reynolds/m

In order to characterize the performance of pulsated injection URANS (unsteady Reynolds-averaged Navier-Stokes) simulations were conducted using the 3.5 million Reynolds/m and a total pressure ratio of 2.081. The frequencies were chosen such that Strouhal numbers (using the length of the separation as the characteristic length) of 1, 0.66, 0.27, and 0.067 were examined (750, 500, 200, 50 Hz respectively). The inlet of flow control was changed to be a sinusoidal mass flow of the form A + A*sin(f*2*pi*t), where f is the frequency, and A is half the mass flow of that seen in the 2.081 pressure ratio case. The same solver settings as for the mesh sensitivity study were used, with a time step of one one-thousandth of the period of excitation. The results showed the greatest acceleration near the crest (highest C_p) for an excitation frequency of 200 Hz which can be seen in figure 2.16. Figure 2.15 shows a schematic of the mass flow signals imposed. Since the average value of the imposed signals is less than the continuous injection, pulsation of this form lowers the mass flow requirements of the injected air.

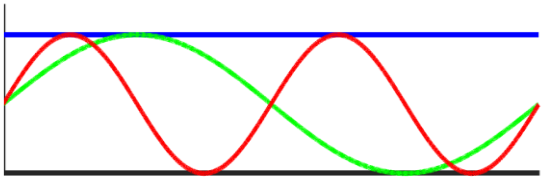

Figure 2.15. Schematic of mass flow signal. Blue represents continuous injection, green 200 Hz injection, and red 400 Hz injection

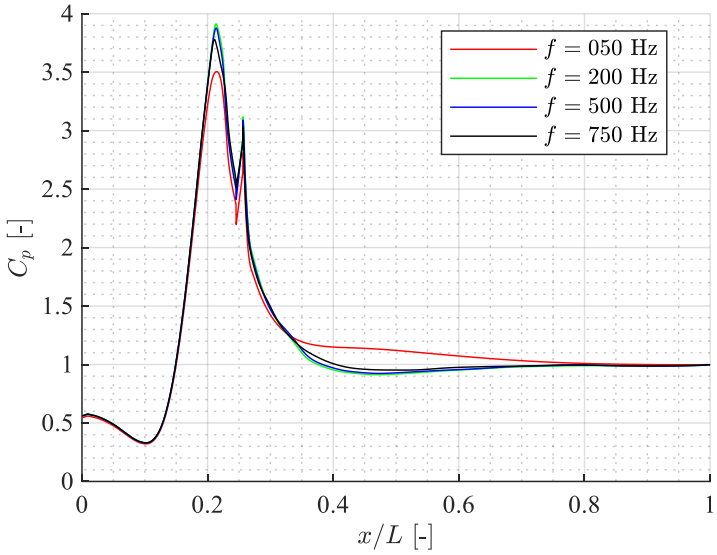

Figure 2.16. Wall Cp response to different frequencies of injection for an inlet Mach number of 0.5 and a Reynolds/m of 3.5 e6

To understand the topology of the pulsated flow injection, time resolved Mach contours were generated. The color map does not change with time so frames can be accurately compared to one another. Figure 2.17 compares time snaps of two frequencies, 50 Hz top and 500 Hz on the bottom. It is shown the flow field alternates between the base flow and the entirely controlled flow field for low frequencies (50 Hz), while for high frequencies (those at and above 200 Hz) shedding is encourages and a rolling separation exists.

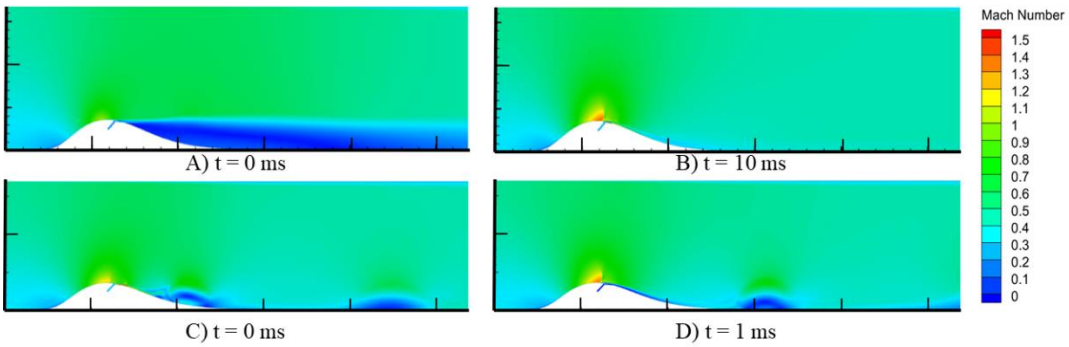

Figure 2.17. Time instance Mach contours for 3.5 million Reynolds /m and a PR of 2.081 A) Separated time instance of 50 Hz injection, B) Controlled instance 1 half period of excitation later, C) Time instance of shedding separation for 500 Hz injection, D) Separation shedding after half a period of excitation

To better understand the effect of discreet blowing ports, a symmetric 3D domain was generated. The central three flow control ports were included. A mesh was generated using HEXPRESS. The side walls were set to be translationally periodic and the inlet conditions of the 3.5 million Reynolds/m case were imposed. As the case proved to be time-varying, all simulations were run with URANS and then time averaged to determine the mean flow conditions. Cell refinements were added until injection ports exhibited symmetric behavior with an inlet total pressure of 70 kPa. Boundary conditions and mesh values are shown in figure 2.18.

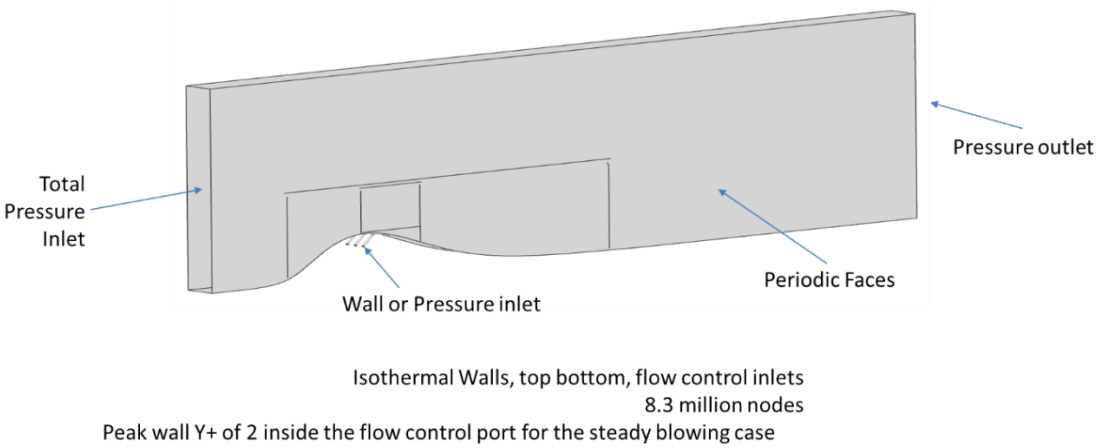

Figure 2.18. 3D Computational Domain

As the mean flow for the 2D case was determined for a range of Reynolds, only the 3,500,000 Reynolds/m case was examined in 3D. The 3D URANS allowed the observation and quantification of the effect of discreet injection on the bulk flow structure. The first immediately obvious conclusion, was that higher total pressures of injection are required to impart the same mass flow and therefore eliminate the SB (Separation Bubble). Selected contours from on simulation with a higher PR than investigated in the 2D case is shown in figure 2.19. For the discrete ports, injected flow tended to lift off of the surface of the wall-mounted hump, seen in figures 2.19 and 2.20. This most likely arises from 3D flow structures not captured by the 2D RANS, resulting in the 2D injection remaining adhered to the bottom wall. However, both the 3D and 2D simulations for steady injection predict a large shock structure just up stream of the injection port (figures 2.12 and 2.20). As a result, the required total pressure ratio for 3D discrete injection is approximately 3.5 times greater than the required pressure ratio required for 2D slot injection.

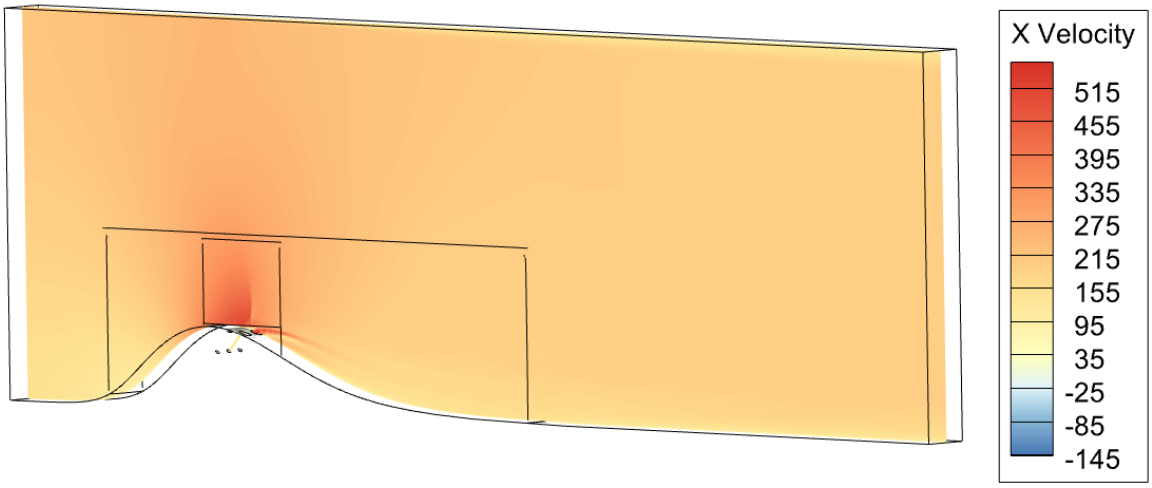

Figure 2.19. Reynolds 3.5 million /m, Control total Pressure ratio = 4; Centerline X Velocity Contour

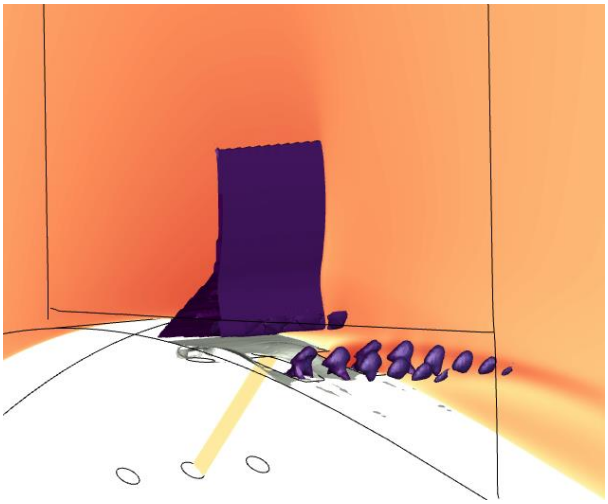

Figure 2.20. Reynolds /m 3.5 million, PR = 4; Purple Shock Surface (as extracted by TecPlot); White Zero x-velocity iso-surface

A test matrix was generated such that Reynolds and Mach numbers that would be seen in low-pressure turbines experiencing increased losses due to separation could be investigated in the PETAL blowdown facility. One-dimensional relationships allowed for the development of said test matrix, with only slight differences in peak Mach numbers du to local curvature or acceleration from flow control. Numerical studies were conducted that show that separation is expected throughout the proposed experimental matrix and that flow injection can be a viable strategy for flow control. Frequencies of excitation were identified with 2D simulations and 3D effects were briefly discussed with 3D simulations. The move towards discrete injection slots meant that higher total pressure ratios were required than the 2D simulations would imply. Pulsated injection did not make a given PR more effective in mitigating separation, however the mass flow required decreases when compared to steady injection.

The above section on the numerical investigation of the test matrix elaborates on sections from a yearly technical progress report for FA9550-19-S-0003 Amendment 001. Similarities between this document and the yearly technical report will exist on the description of the RANS and URANS results and figures.

3. ANALYSIS OF EXPERIMENTAL RESULTS

The inlet measurements were used to quantify inlet Mach number and Reynolds numbers according to equations below. A two tenths of a second region in time, where the average Mach number is a value of interest, is found and the Reynolds number over that interval is averaged. Wall pressure taps were averaged for two tenths of a second and translated to Cp, defined below. The Cp followed the same trend that was seen in the isentropic Mach number, as discussed in section 2.4 (e.g. figures 2.11 (left) and 2.12 (left)), where sudden deviations of slope towards horizontal represent detached flow. The uncertainty of derived quantities was calculated using the discrete approach on the partial derivative expansion, as done in Moffat (1988). Variations in total temperature achieved in the test section, due to varying prior test duration, ambient temperature, or instant in a given blowdown could cause some deviation in Cp, which was not quantified.

$$M = \sqrt{\left(\left(\frac{P_{0,inlet}}{P_{s,inlet}}\right)^{\frac{\gamma-1}{\gamma}} - 1\right) * \frac{2}{\gamma - 1}}$$

$$T = T_{0,inlet} * \left(1 + \frac{\gamma - 1}{2} * M^2\right)^{-1}$$

$$\mu = \mu_{ref}\left(\frac{T}{T_{ref}}\right)^{3/2}\frac{T_{ref} + S}{T + S}$$

$$Reynolds\ /m = \frac{P_{s,inlet}}{RT} * \frac{M * \sqrt{\gamma RT}}{\mu}$$

$$C_p = \frac{P_{0,inlet} - P_{s,local}}{P_{0,inlet} - P_{s,exit}}$$

3.1 Test Condition Analysis

This section serves to explain how conditions in the test article evolved over time. The quantities calculated from the equations above were calculated for each data sample. This provided a time history of inlet Mach and Reynolds numbers throughout each experiment. Due to the time frame in which the purge valve, and fast-acting valve into PT1 are open, there was a brief impulse of mass flow into the test article greater than prescribed by the high-pressure piping. This was due

to below atmospheric pressures in the low-pressure piping. The data showed a large spike total pressures, and pressures upstream of the crest of the hump, as well as a sharp valley in the pressure at the crest and exit pressures, taken at the farthest downstream pressure tap. The total temperature slowly rises over the course of the blowdown. All this can be seen in figure 3.1 below.

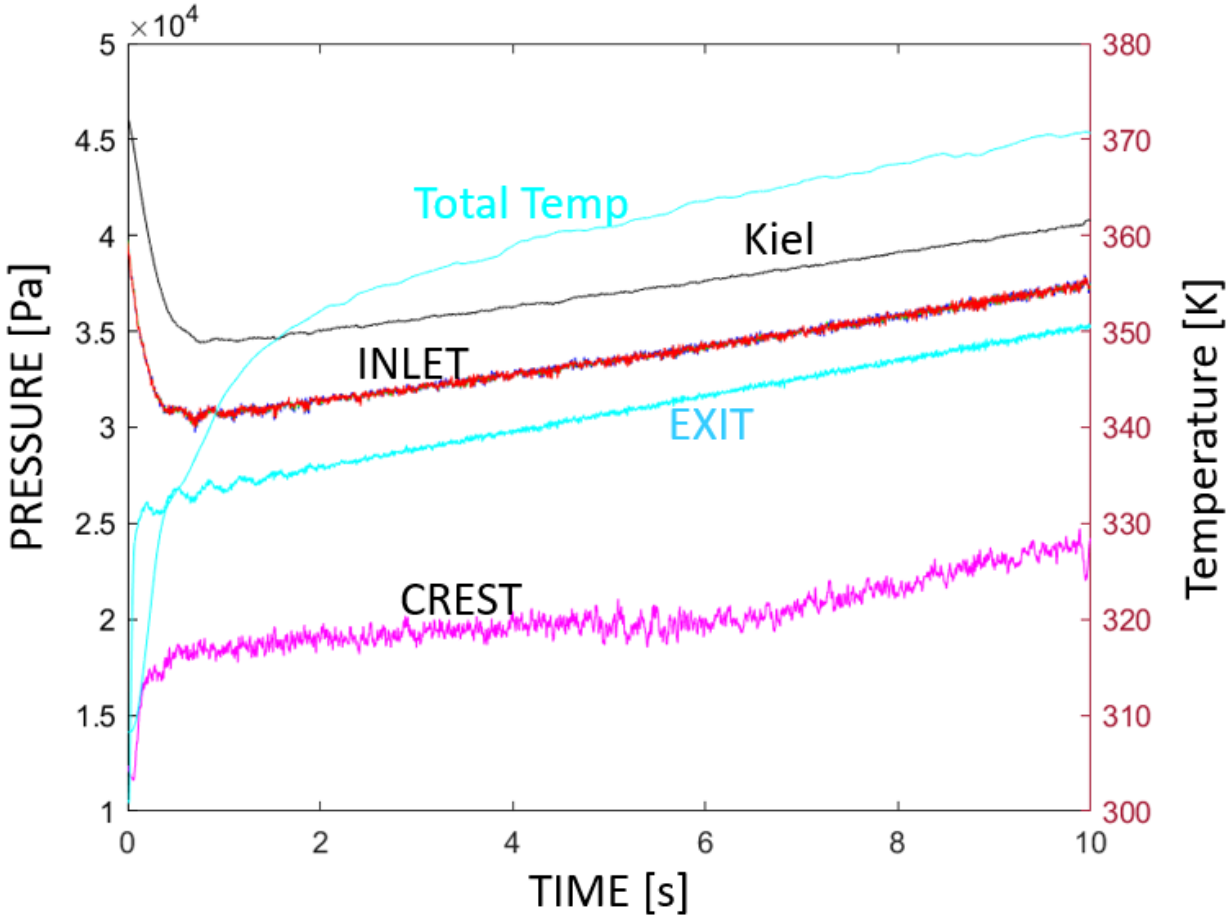

Figure 3.1. Time traces of inlet total temperature, total pressure, static temperature, crest static pressure and exit pressure for a representative blowdown

Similarly, Reynolds and Mach numbers were shown for repetitions of the same target conditions, once without flow injection, and once with steady injection. The plots show what was anticipated in section 2.3, Mach would spike and decrease steadily, while Reynolds would spike and decay, but at a very slow pace. One reason, the spike in Mach is not as distinct as the spike in Reynolds, is the temporal uncertainty as a result of different length pneumatic lines. During startup, the total pressure signal may have been lagging behind the static pressure signal, leading to potentially imaginary isentropic Mach numbers. However, once the start-up transience was

completely finished, the potential temporal misalignment in total and static pressures is greatly diminished as the total pressure changes slowly.

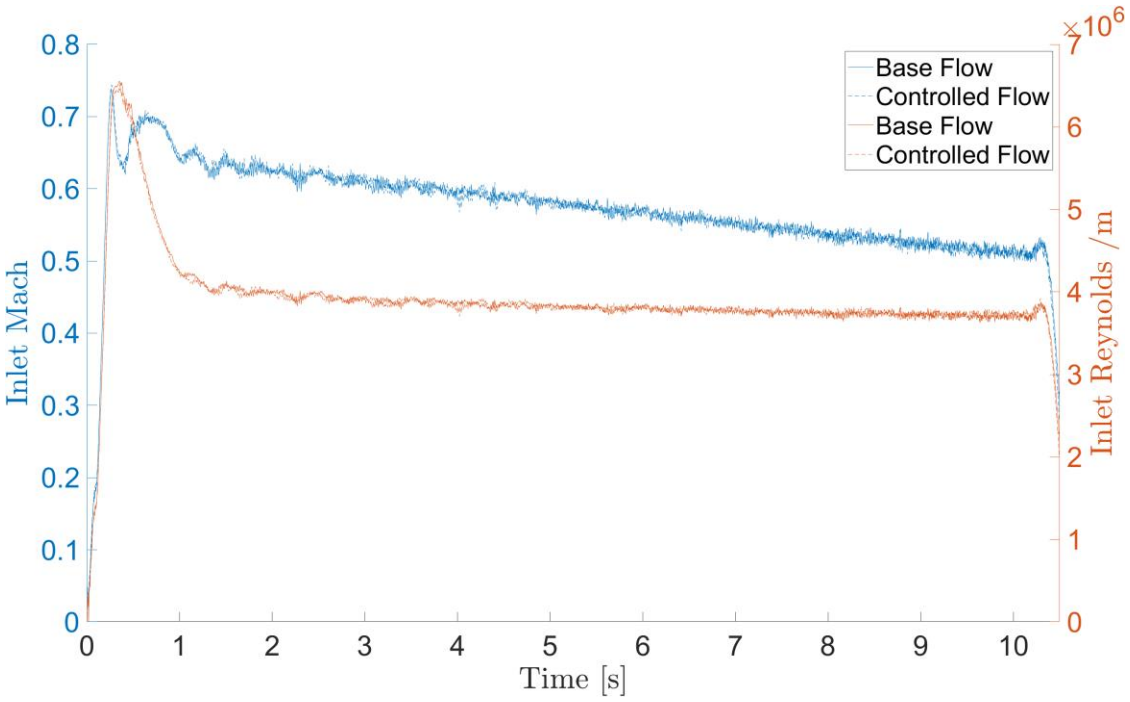

Figure 3.2. Representative time trace of inlet Mach and Reynolds for a paired base and controlled flow

Appendix B shows the Reynolds number, inlet Mach number, injection total pressure ratio and injection frequency (if applicable) for all blow-down experiments to be discussed. The range that was experimentally investigated was approximately 600,000 Reynolds/m greater than what was originally targeted (shown in table 2.1), mostly due to depressed total temperatures for the reasons stated in section 2.3. Since the heater increases the time to establish flow conditions, an equivalent set of conditions with no heating requirement were found and used to investigate the effects of pulsated injection. Each case name in Appendix B starts with an “H” for heater or “N” for no heater and ends in -XX-YYY. Where X is the blowdown number used for that heated or unheated case and YYY is the time in the blowdown at which the data was averaged in hundredths of seconds.

3.2 Uncertainty Quantification

Pressure coefficient ($C_{p)}$, inlet Mach, inlet Reynolds /m, and PR are discussed, all of which were derived from measurements taken during the experimental campaign. Uncertainties were quantified using the method laid out by Moffatt (1988). Where the contribution to the change of the derived quantity from the mean value plus the absolute uncertainty of the measurement is calculated for every measured or assumed quantity (derived quantity calculated using mean plus uncertainty). The percent difference due to this change is considered the variation with respect to the mean of the derived quantity in percent. The variation divided by the relative uncertainty of the measurement is the sensitivity of the derived quantity to each measurement. The relative uncertainty in the derived quantity is the root mean square of the variation in the derived quantity for each measured quantity. The 95% confidence band of the derived quantity is then calculated as the relative uncertainty times the mean value of the derived quantity. This process is shown for one measured quantity which contributes C_p, in appendix D.

The lowest pressure and temperature blow-down (N-15-772) was chosen to tabulate these uncertainties as the relative errors in total temperature and pressure would be highest. The crest is chosen as the location to tabulate errors in C_p as the magnitude of the pressure at the crest is the lowest in magnitude most often, due to the elevated velocity. Tables 3.1 through 3.4 show the uncertainty in C_p, inlet Mach, inlet Reynolds /m, and PR respectively. The tabulated values are a conservative estimate for the errors in all derived quantities shown.

All relative uncertainties in derived quantities are below 2%, so a more rigorous approach to quantify uncertainties was not attempted. Charts throughout sections 3.3 and 3.4 will not have error bars to increase readability. Tables 3.2 and 3.3 show derived quantities were most sensitive to the value of gamma used in their calculations. Similarly, Reynolds /m is largely sensitive to total pressure over the other measured quantities, emphasizing the importance of accurate thermocouple calibrations.

Table 3.1. Uncertainty in CP

Quantity	Mean Value	Units	Absolute Uncertainty	Uncertainty in % mean	C_p calculated using Mean + uncertainty	Variation of C_p with respect to Mean in %	Sensitivity of C_p to Quantity
$P_{0,inlet}$	32123	Pa	200	0.62%	3.103	-2.30%	-3.70
$P_{s,local}$	13853	Pa	50	0.36%	3.167	-0.27%	-1.32
$P_{s,exit}$	26371	Pa	50	0.19%	3.204	0.88%	0.22
		$C_{p,crest}$	3.176	Relative Uncertainty of $C_{p,crest}$	1.43%	95% band +/- 0.045	

Table 3.2. Uncertainty in inlet Mach

Quantity	Mean Value	Units	Absolute Uncertainty	Uncertainty in % mean	Inlet Mach calculated using Mean + uncertainty	Variation of Inlet Mach with respect to Mean in %	Sensitivity of Mach to Quantity
$P_{0,inlet}$	32123	Pa	200	0.62%	0.583	1.42%	0.44
$P_{s,inlet}$	25674	Pa	50	0.19%	0.572	-0.45%	-0.43
gamma	1.4	-	0.05	3.57%	0.566	-1.60%	-2.23
		M	0.575	Relative Uncertainty of M	1.26%	95% band +/- 0.007	

Table 3.3. Uncertainty in inlet Reynolds /m

Quantity	Mean Value	Units	Absolute Uncertainty	Uncertainty in % mean	Reynolds/m calculated using Mean + uncertainty	Variation of Reynolds/m with respect to Mean in %	Sensitivity of Reynolds to Quantity
$P_{0,inlet}$	32123	Pa	200	0.62%	3887074	1.65%	0.38
$P_{s,inlet}$	25674	Pa	50	0.19%	3811397	-0.33%	-0.60
$T_{0,inlet}$	283	K	3	1.06%	3772368	-1.35%	-0.79
gamma	1.4	-	0.05	3.57%	3856775	0.86%	4.15
		Re /m	3823881	Relative Uncertainty of Re /m	1.16%	95% band +/- 44398	

Table 3.4. Uncertainty in PR

Quantity	Mean Value	Units	Absolute Uncertainty	Uncertainty in % mean	PR calculated using Mean + uncertainty	Variation of PR with respect to Mean in %	Sensitivity of PR to Quantity
$P_{0,inlet}$	32123	Pa	200	0.62%	2.686	-0.62%	-0.99
$P_{0,injected}$	86827	Pa	200	0.23%	2.709	0.23%	1.00
		PR	2.703	Relative Uncertainty of PR	0.47%	95% band +/- 0.013	

3.3 Base Flow

The pressure coefficient from the pressure taps was used to characterize the bulk separation, qualitatively. It was observed the SB grew in size when the inlet Mach number increases or the inlet Reynolds number decreases (figures 3.3 and 3.4 respectively). The surface contour of the 3D hump is plotted for reference on the independent y axis to the right.

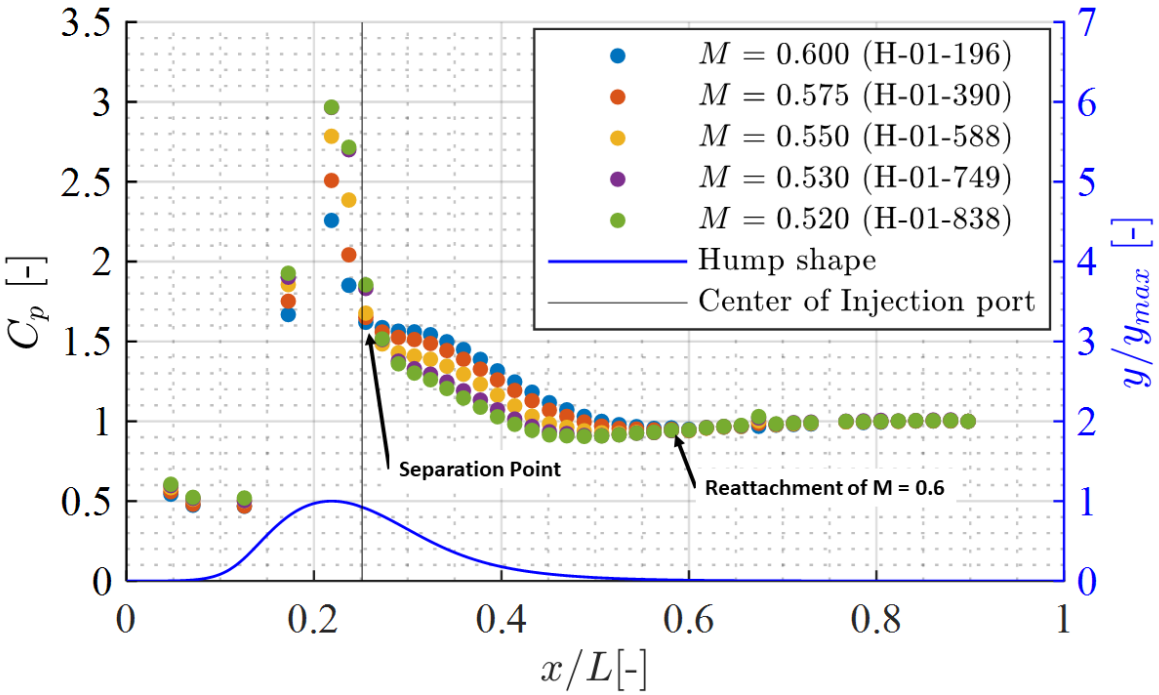

Figure 3.3. Growth of separation with increasing inlet Mach numbers

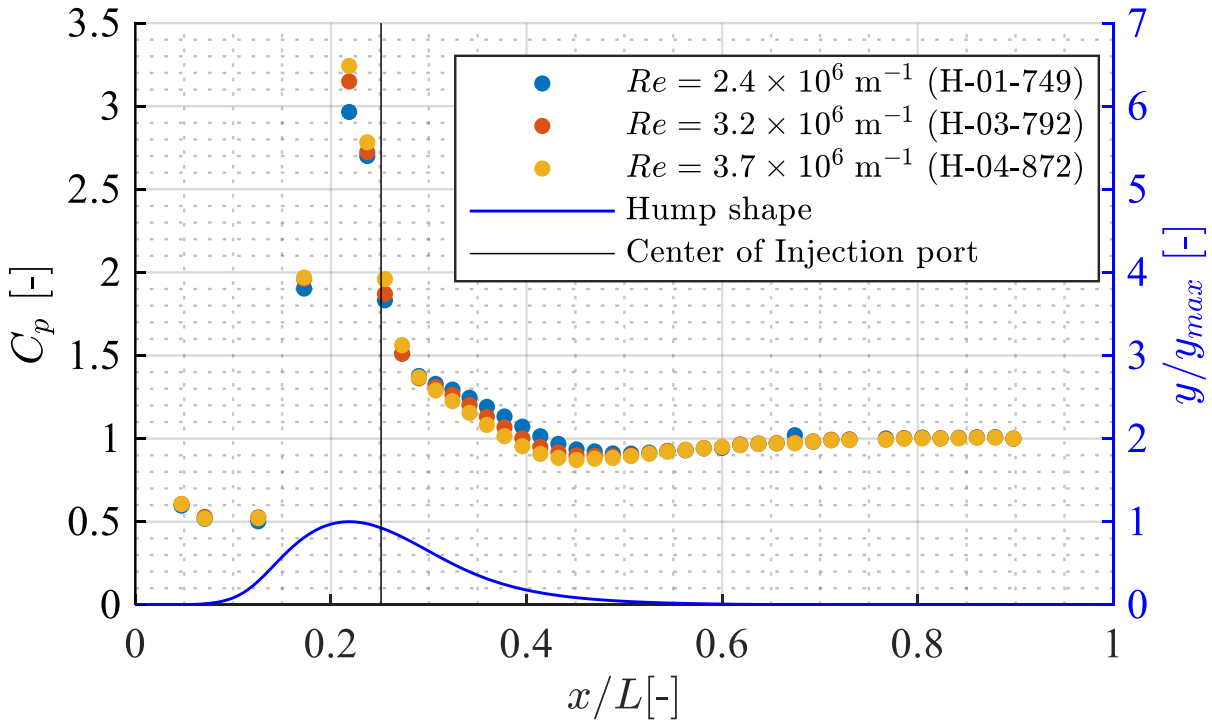

Figure 3.4. Growth of separation with decreasing inlet Reynolds Numbers

The start-up transience of the base flows was assessed through a linear schlieren set-up looking at the crest (region 1) with a 10 kHz frame rate. The footage revealed weak shocks forming as the separation formed, then a relatively consistent separation point and region was established. Both features are observed as a dark region in the schlieren imaging. Figure 3.5 shows four-time instances, showing the formation and stabilization of the laminar separation bubble.

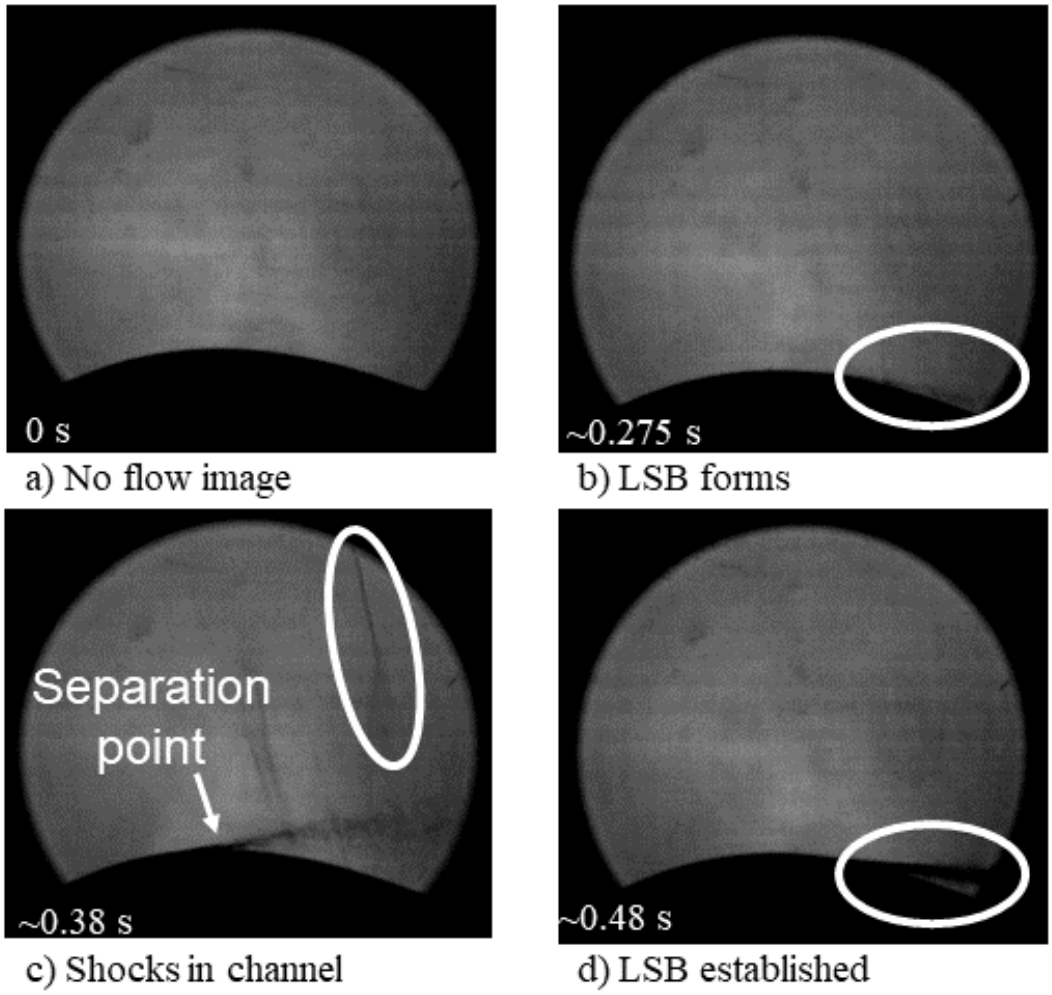

Figure 3.5. Linear Schlieren of region 1 during start-up transience

Another instance of schlieren with the same set-up was triggered eight seconds later in the test. This sequence of images made it clear the separation is weaker at this point in the test, when the inlet Mach number has decreased. Similarly, as in figure 3.5, sporadically shocks appear near the crest, this time at attached to the surface of the test article. An image of the weaker separation and the stronger shock along the bottom wall are shown in figure 3.6. the shocks most likely appear due to blockage in the channel associated with the shear layer above the separation. Once the shock forms the shear layer elevates into the lower total pressure region and the blockage increases, thereby increasing the blockage and moving the local shock farther upstream.

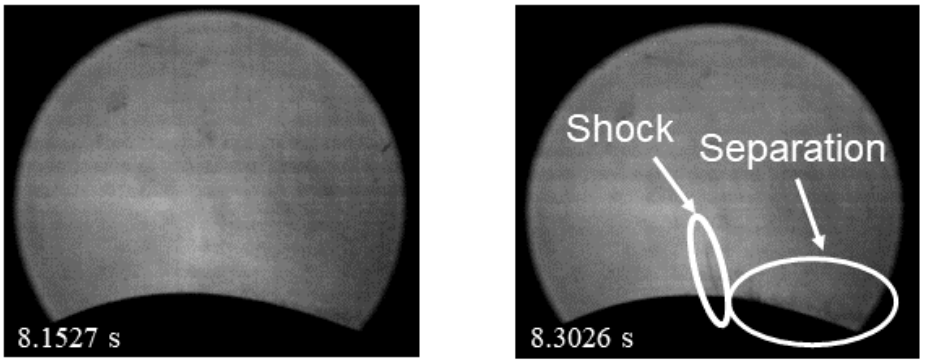

a) Weak separation b) Shock plus stronger Separation

Figure 3.6. Linear Schlieren of region 1, 8 seconds into a blowdown

3.4 Controlled Flows

After the base flow was well understood, flow control in the form of flow injection was added in two phases. First steady injection was explored experimentally, then the benefits of pulsation were investigated. The Cp distribution along the bottom wall was used to characterize the response of the separated region to steady and pulsated injection. Using the simulations discussed in section 2.4 as a reference, pressure ratios of injection between 1.4 and 3.92 were explored for steady injection, while pressure ratios near 3.5 were targeted for pulsated injection. The differential pressure limitation of the FESTO valves and the manifold that supplied the injection ports limited the lower bound of pressure ratios experimentally investigated.

The Cp distribution shows the laminar separation bubble responds to the lowest injection pressures explored and is impacted greater by larger injection pressures. An injection total pressure ratio near 2 seems to have suppressed the majority of the separation, though increasing PR beyond 2 does yield some diminishing benefit. Pressure ratios near 3 seem to have almost fully mitigated the separation. Figure 3.7 plots the Cp distribution for various pressure ratios against a simulation conducted by Federico Lluesma-Rodriguez for a parallel numerical work. The simulation used the boundary conditions imposed experimentally and is shown with a solid line. The chart implies that the threshold for completely effective steady injection is a pressure ratio that lies between 2 and 2.9. Using the highest pressure ratio investigated and the isentropic equation for choked flow, the maximum injected flow rate as a percentage of the mass flow through the inlet of the test article was approximately 2.9%.

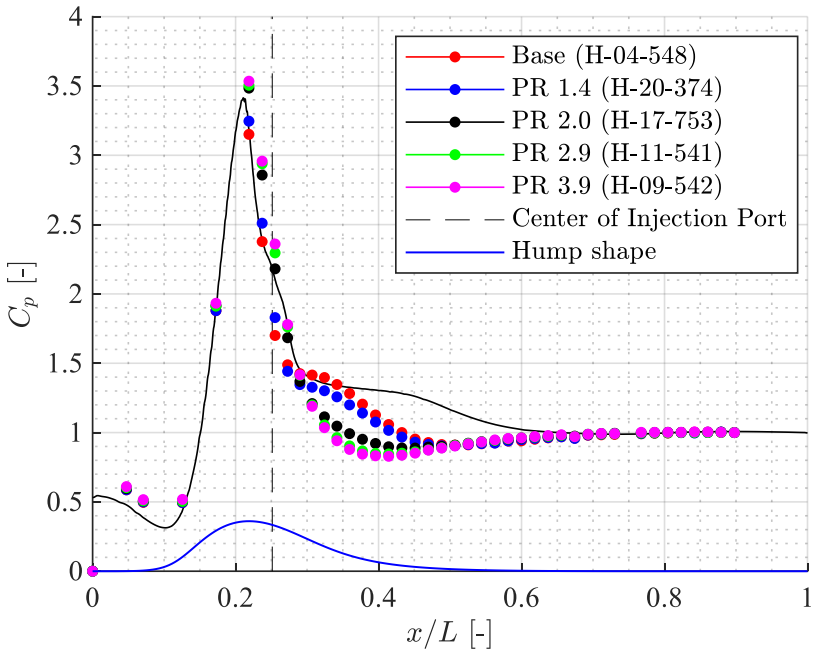

Figure 3.7. Wall Cp response to steady injection for approximately 3.8 e 6 Reynolds /m with an inlet Mach number of 0.575

The flow features were investigated using a linear schlieren set up with a 2 kHz frame rate at schlieren region 2. The schlieren images make the effectiveness of steady injection through transient and steady processes clear. Approximately, the first second of a given experiment was marked by a start-up transience that was linked with supersonic flow of the 3D hump that quickly returns to transonic. Throughout this start-up transience the injection port was over-powered by the SB and eventual formation of the injection leading edge shock, as seen in figures 3.8.b and 3.8.c. Then, a second shock forms with a separation the starts downstream and migrates towards the crest (figure 3.8.d). This separation is affected in some way by the injection. Once the supersonic separation was upstream of injection ports (figure 3.8.e) the inlet Mach began to fall and the injection leading edge shock disappears. At around 0.85 seconds, the strong shocks near the crest no longer formed and the transonic SB began to interact with the imposed steady injection (figure 3.8.f) which weakened its strength relative to the shear layers that had previously formed. After approximately 4 seconds, the streams from the injection ports have grown in relative strength, indicated by the visible plume length, but was coupled with a lambda shock and upstream separation (figure 3.8.i). Figures 3.8.j through 3.8.l show a time period between 5 and 10 seconds

in which the flow from the injection port remained stable with a small separation appearing sporadically upstream, but being eliminated by the injected flow.

As the injection pressure throughout the blow-down shown in figure 3.8 is constant, the injection total pressure ratio slowly decreased due to the increase in total pressure over time. This effect however, was significantly weaker than the decrease in size of the separation as the Mach number decreased as the blow-down evolved. The length of the uncontrolled separation and the minimum total pressure ratio required to mitigate separation entirely is tabulated below (in table 3.5) for one Reynolds number and several Mach numbers.

Table 3.5. Optimum Pressure Ratios as a function of separation length

Name base	$\boldsymbol{Re}$ **[m^{-1}]**	$\boldsymbol{M}$ **[-]**	**SB [m]**	**PR opt. [-]**
H-04-381	3.9×10^6	0.600	0.136	2.54
H-04-548	3.9×10^6	0.575	0.117	1.71
H-04-708	3.8×10^6	0.550	0.115	1.64
H-04-872	3.8×10^6	0.530	0.106	1.61

Steady injection served to examine the effects of total pressure on injection and identify an effective threshold. Pulsation was then applied to three pressure ratios above the effective threshold. Two which were closer to the lower bound of the threshold identified in figure 3.7, and one which was elevated to investigate a range of frequencies in a regime the FESTO valves could impose reliably.

A range of frequencies between 50 and 400 Hz were experimentally imposed to the injection ports. The Cp distribution along the bottom wall of the test-article was analyzed to determine the response of the separation bubble. It also was observed that the efficacy of the pulsation increases with frequency (figure 3.10). There was little to no bulk separation when the frequency of pulsation was at or above 200 Hz for effective pressure ratios, though diminishing benefits start to appear near 125 Hz oscillation. Figure 3.10 further refines the bounds of the effective PR to be between 2.12 and 2.70.

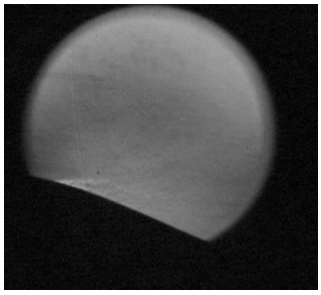

a) Time = 0 [s]
Injection port flow only

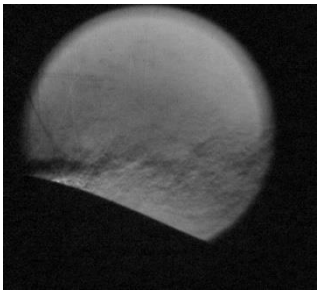

b) Time = 0.1760 [s]
SB begins to establish

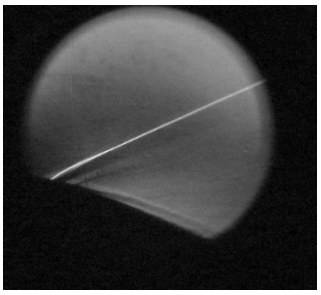

c) Time = 0.2635 [s]
Oblique shock formation

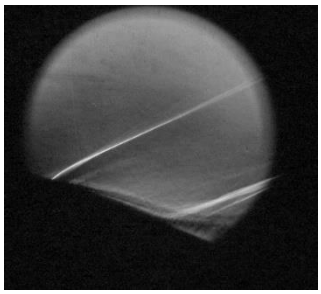

d) Time = 0.4300 [s]
SB grows toward inlet

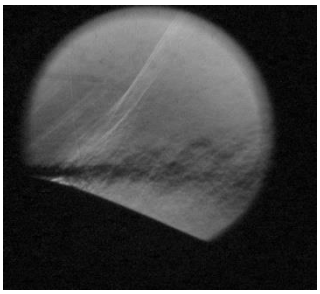

e) Time = 0.4840 [s]
Throat becomes transonic

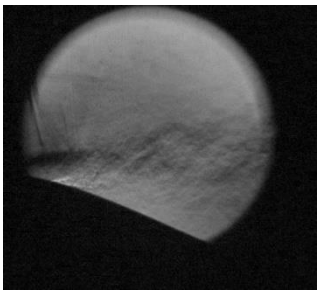

f) Time = 0.5580 [s]
SB forms lambda shock

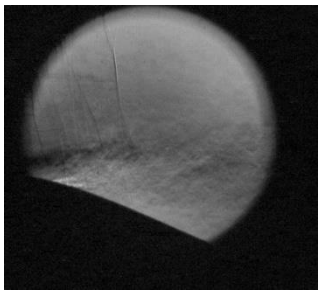

g) Time = 0.6735 [s]
Separated weak shock

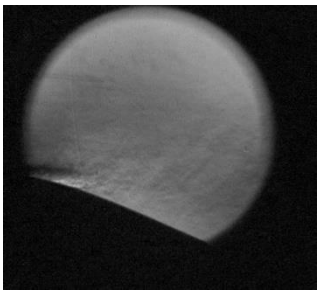

h) Time = 0.8440 [s]
SB interacts with injection

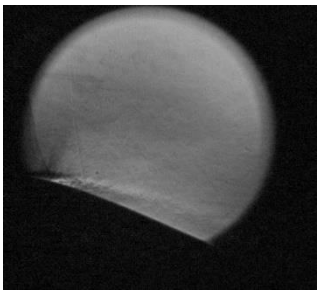

i) Time = 4.4135 [s]
Injection adheres to surface

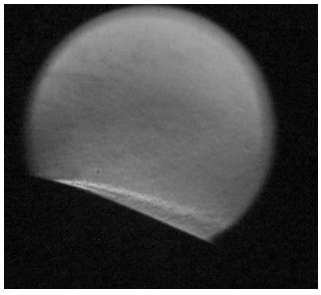

j) Time = 5.3510 [s]
SB formation abated

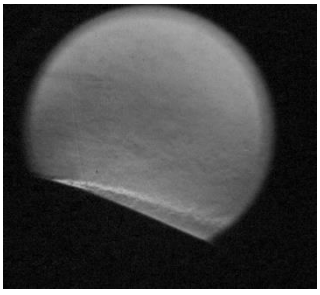

k) Time = 6.4695 [s]
SB formation abated

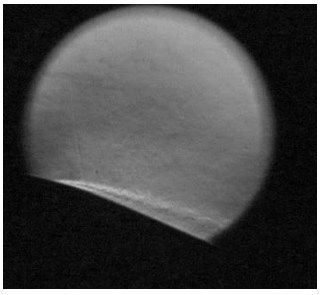

l) Time = 8.0935 [s]
SB formation abated

Figure 3.8. Schlieren imaging of steady injection with linear set-up in region 2.

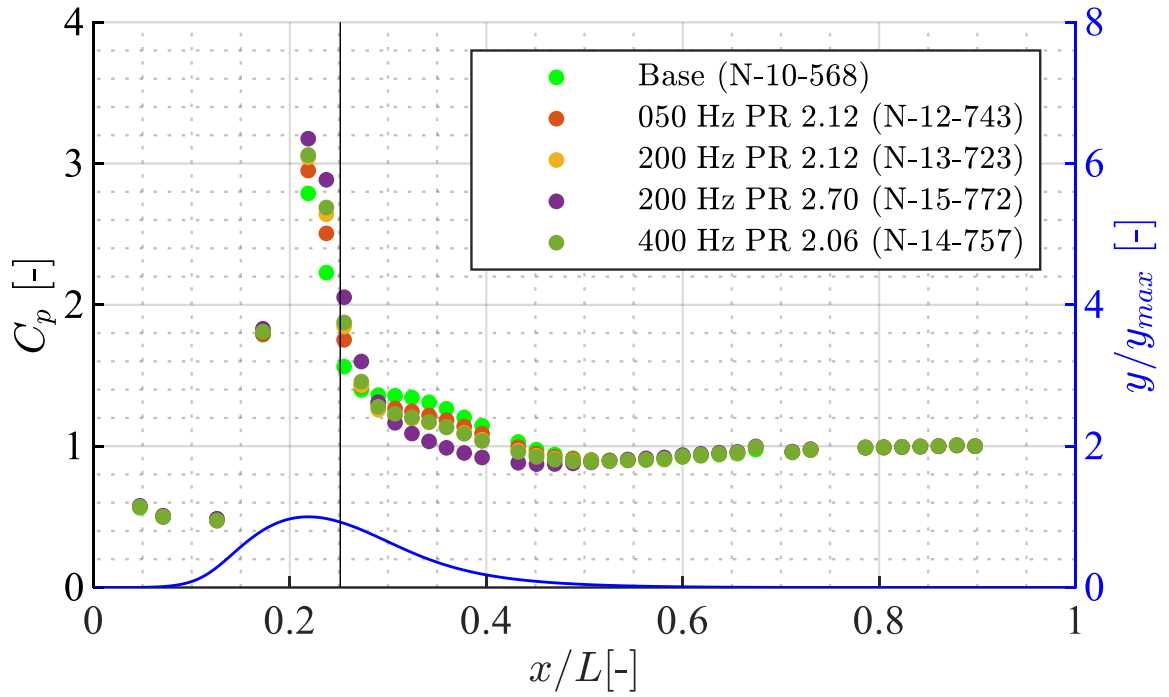

Figure 3.9. Bottom wall Cp distribution response to different frequencies and pressure ratios

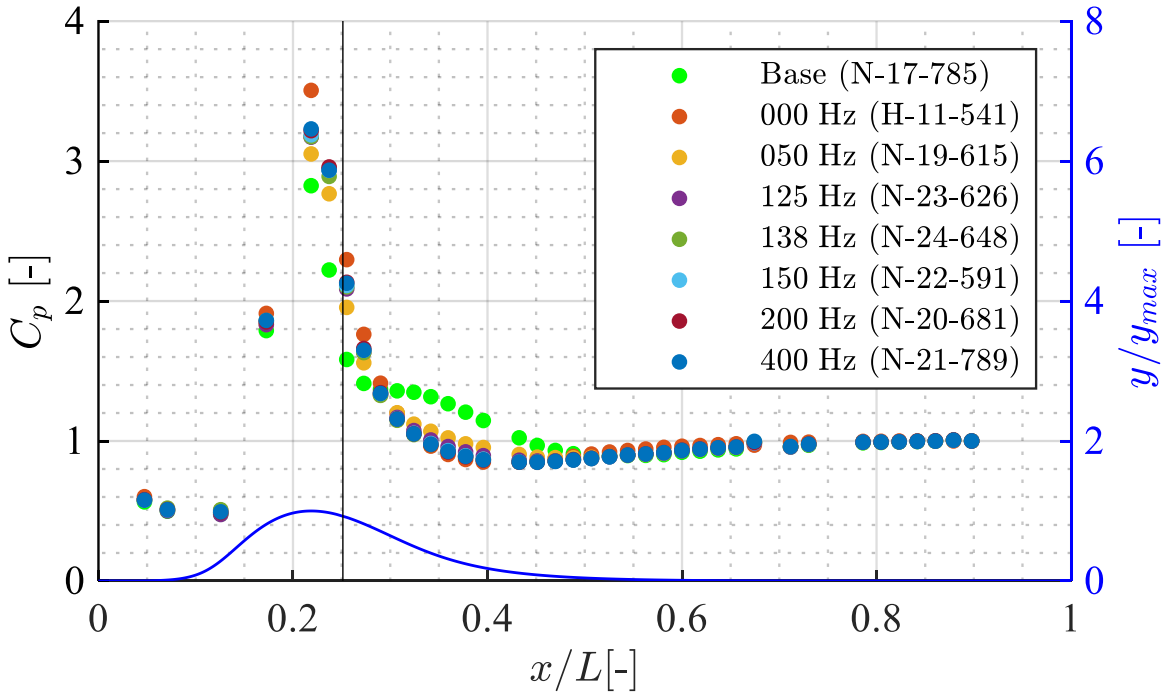

Figure 3.10. Bottom wall Cp distribution response to different frequencies of pulsation for a PR of approximately 3.6

Schlieren imagery was used in an attempt to qualitatively identify flow features of the pulsated injection cases. A z-type set-up was used in region 3 with a framerate of 4000 Hz. Due to the nature of z-type, the sensitivity was increased, but the set-up used had significant aberrations on the right side of the images. A background is included for reference for the schlieren images shown. All images are shown for no heater blowdown 15 which is a case with effective pulsated injection, at a time near the one plotted in figure 3.11. The dark region near the crest of the hump is indicative of flow structures. The flow field oscillated between the controlled and uncontrolled state, not the continuously shedding separation seen in section 2.4. The dark plume which follows the surface of the hump at some offset is the entrained shear layer, while the light region on the surface is the flow injected. This also shows the wall pressure taps resolve a time-averaged flow field, and not the complex topology along the wall.

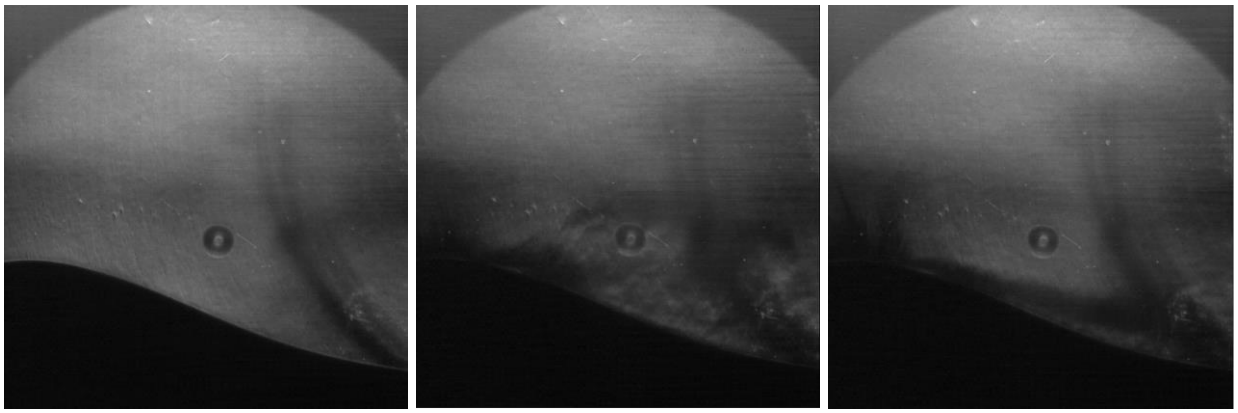

Figure 3.11. Schlieren imaging of pulsated injection for no heater blowdown 15. From left to right, a background image with no flow through the test article, an instance where the injection overpowers the separation and an example at which the separation is present

4. CONCLUSIONS

The objective of this thesis, the **demonstration of separation abatement through steady and pulsated flow injection**, has been achieved through the application of a combined experimental and numerical methodology. An existing test article was modified to include features necessary for the implementation of flow control. By developing a test matrix with both 1D relationships and the employment of low fidelity computational methods, a suitable regime for applying flow control was found and experimentally explored. Flow injection as a strategy to control quasi-2D separation has been experimentally evaluated in a transonic regime, showing the methodology followed was successful in adequately designing a relevant experiment. The time-averaged response of a bulk separation was assessed using pressure taps while unsteady features were qualitatively identified through various schlieren imagery set-ups.

Numerical studies provided some insight into flow topologies, but failed to accurately predict the extent of the separation compared to experimental data for the same Mach and Reynolds numbers. The experimental campaign investigated higher inlet Mach numbers than initially planned, to ensure a sizable separated region was present. These numerical studies also failed to accurately predict the required pressure required for injection. This was due to the fact that a continuous slot is modeled for a 2D simulation and that the 3D slots may have complex flow fields that were not resolved in the steady simulations conducted.

Steady injection proved to be an effective method to mitigate separation experimentally. This is seen both through Cp distributions, and through the lack of a separated shear layer present in the schlieren imaging shown for a representative blowdown.

Unsteady injection was also shown to be an effective method in mitigating separated flow. Though 2D numerical studies failed to model the features accurately, they accurately found effective injection frequencies. The pressure required for effective control was similar to that required by steady injection. The addition of pulsation reduces the overall mass flow required, for the signals imposed by this study. This is beneficial if the source of the air used for injection is bled from the device in which flow control is intended. Additional efforts to characterize potential attenuation of the imposed pulsation by the ports themselves could provide added insight on the design of features for flow control via injection.

The major conclusions can be condensed to the following list:

- There is an optimum injection total pressure ratio where the losses from the separation and the mixing caused by a shock are minimized.
- Two-dimensional simulations can effectively guide the determination of injection frequencies.
- Required injection quantities need to be analyzed based on the flow injection port geometry, or should be normalized with a different quantity than total pressure ratio.
- Steady and pulsated injection are viable strategies in mitigating separation in transonic, internal flows.
- Pulsation did not make an injection pressure more effective in mitigating separation.
    - There may be an optimum frequency; however, asymptotic behavior was observed as frequencies increased.
    - For signals with lower mean total pressures than steady injection, the mass flow requirement is reduced when compared to steady injection.

Future studies should attempt to generalize the findings presented above. Total pressure ratio of injection works well to compare the performance of a singular injection geometry, but does not compare two disparate geometries together well. As seen by the requirement of larger total pressure ratios in the experiments and 3D simulations when compared to the 2D simulations (discrete port compared to slot injection). The role of the Strouhal number in identifying an optimum frequency across many flow regimes should also be investigated

Additionally, work should be done to enhance the understanding of how the flow structure of the injected flow enhances or diminishes the mitigation of separation. The injection ports used experimentally likely have a complex flow structure due to the change in direction and cross section near the interface with the surface of the wall-mounted hump. These structures are almost definitely impacting the behavior of the injected jet, and the understanding of this phenomenon would aid future designers in the design of flow control system.

The experiments conducted showed an entanglement between the separation and shocks which formed in the test article. It is likely that shock-boundary layer interactions alter or impact the mechanisms of separation, and efforts to understand these effects could similarly aid in the design of flow control systems.

As flow separation in a low-pressure turbine airfoil is likely not quasi-2D, additional studies on how to best locate and angle flow injection ports in 3D separations should be conducted. Similarly, once flow control in a propulsion device is demonstrated, the impact of the bleed air used for flow control on the propulsion cycle should be quantified, as well as the potential effects on structural components, noise, and other implementation specific effects of the implementation of flow control.

APPENDIX A. MECHANICAL DRAWINGS

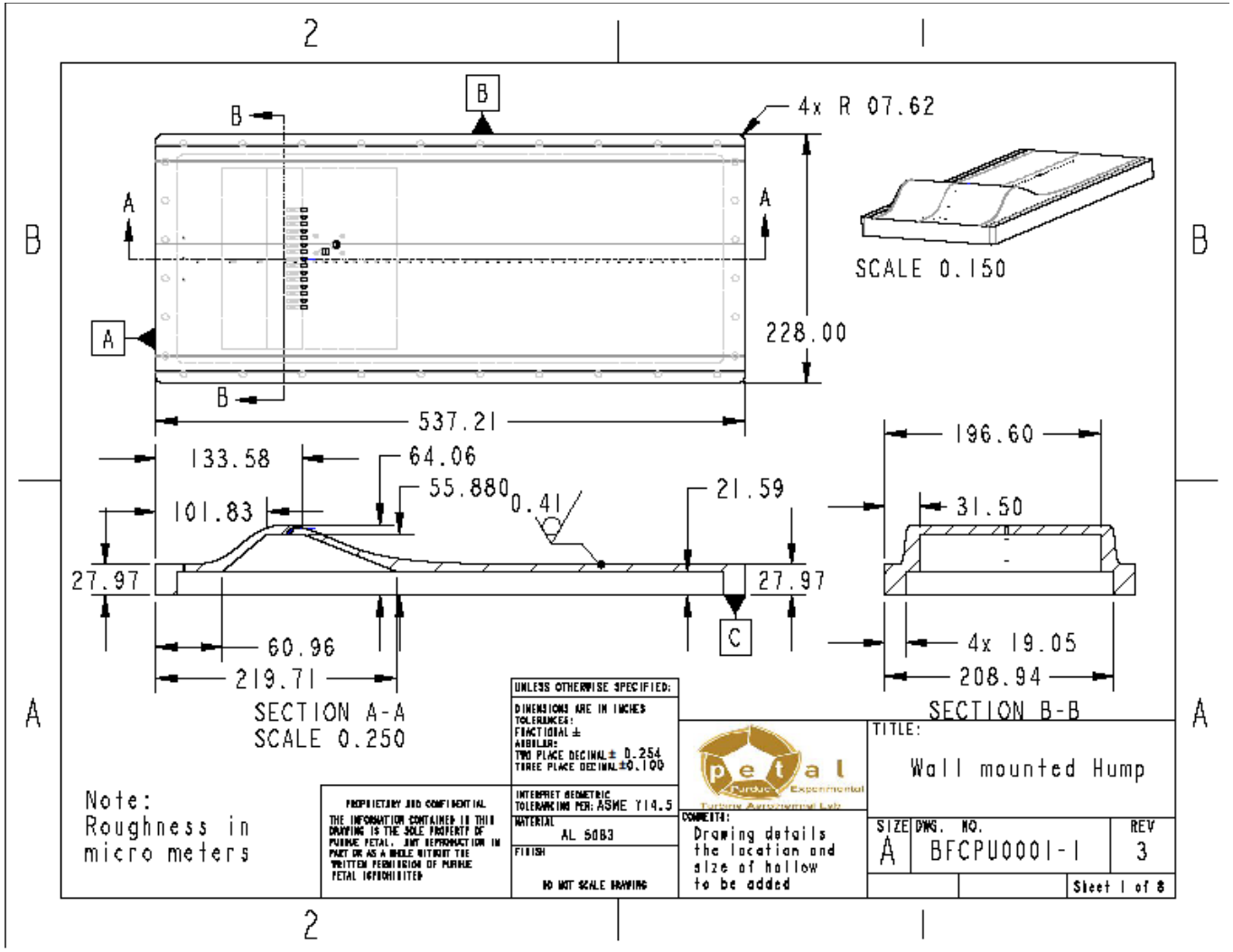

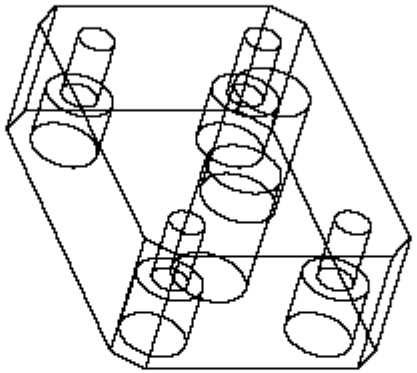

UNLESS OTHERWISE SPECIFIED:

DIMENSIONS ARE IN INCHES
TOLERANCES:
FRACTIONAL ±1/64
ANGULAR: ± 0.1°
TWO PLACE DECIMAL ±0.02
THREE PLACE DECIMAL ±0.004

INTERPRET GEOMETRIC TOLERANCING PER: ASME Y14.5

MATERIAL
AL 5083

FINISH

DO NOT SCALE DRAWING

COMMENTS:

TITLE:

Mounting Bracket

SIZE	DWG. NO.	REV
A	BFCPU0001-2	5

Sheet 1 of 3

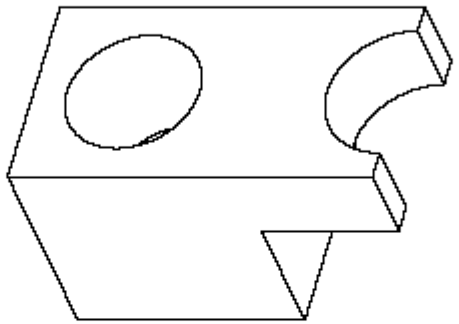

SCALE 4.000

UNLESS OTHERWISE SPECIFIED:

DIMENSIONS ARE IN INCHES
TOLERANCES:
FRACTIONAL ± 1/32
ANGULAR: ±0.1°
TWO PLACE DECIMAL ±0.01
THREE PLACE DECIMAL ±0.004

INTERPRET GEOMETRIC TOLERANCING PER: ASME Y14.5

MATERIAL
AL

FINISH

DO NOT SCALE DRAWING

DRAWN:
Isometric View

TITLE:
Mounting Clamp

SIZE	DWG. NO.	REV
A	BFCPU0001-3	1

Sheet 1 of 2

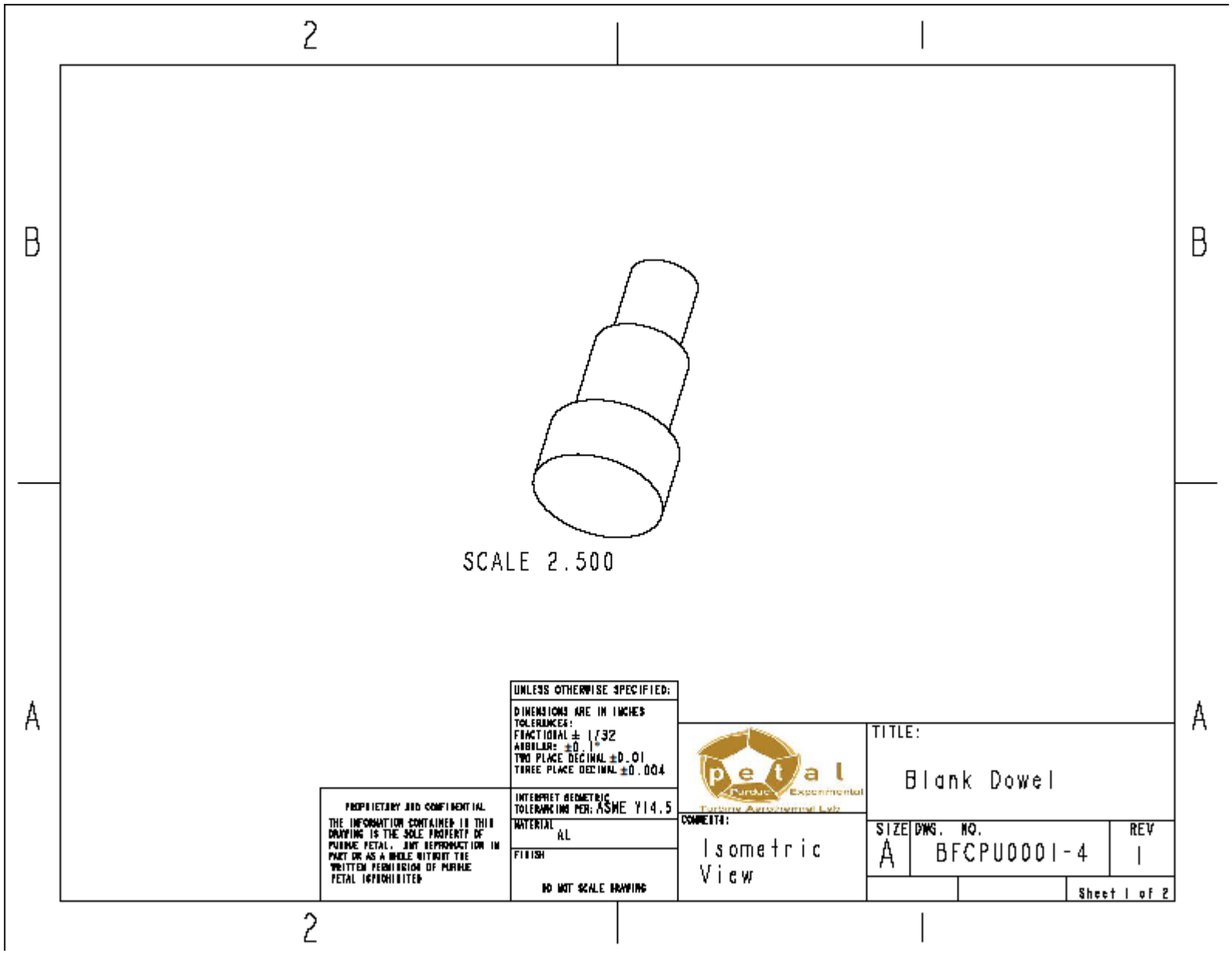
2
1
B
A
SCALE 2.500
UNLESS OTHERWISE SPECIFIED:
DIMENSIONS ARE IN INCHES
TOLERANCES:
FRACTIONAL ± 1/32
ANGULAR: ±0.1°
TWO PLACE DECIMAL ±0.01
THREE PLACE DECIMAL ±0.004
INTERPRET GEOMETRIC TOLERANCING PER: ASME Y14.5
MATERIAL
AL
FINISH
DO NOT SCALE DRAWING
PROPRIETARY AND CONFIDENTIAL
THE INFORMATION CONTAINED IN THIS DRAWING IS THE SOLE PROPERTY OF PURDUE PETAL. ANY REPRODUCTION IN PART OR AS A WHOLE WITHOUT THE WRITTEN PERMISSION OF PURDUE PETAL IS PROHIBITED
petal
Purdue Experimental
Future Aerospace Lab
COMMENTS:
Isometric View
TITLE:
Blank Dowel
SIZE
A
DWG. NO.
BFCPU0001-4
REV
1
Sheet 1 of 2

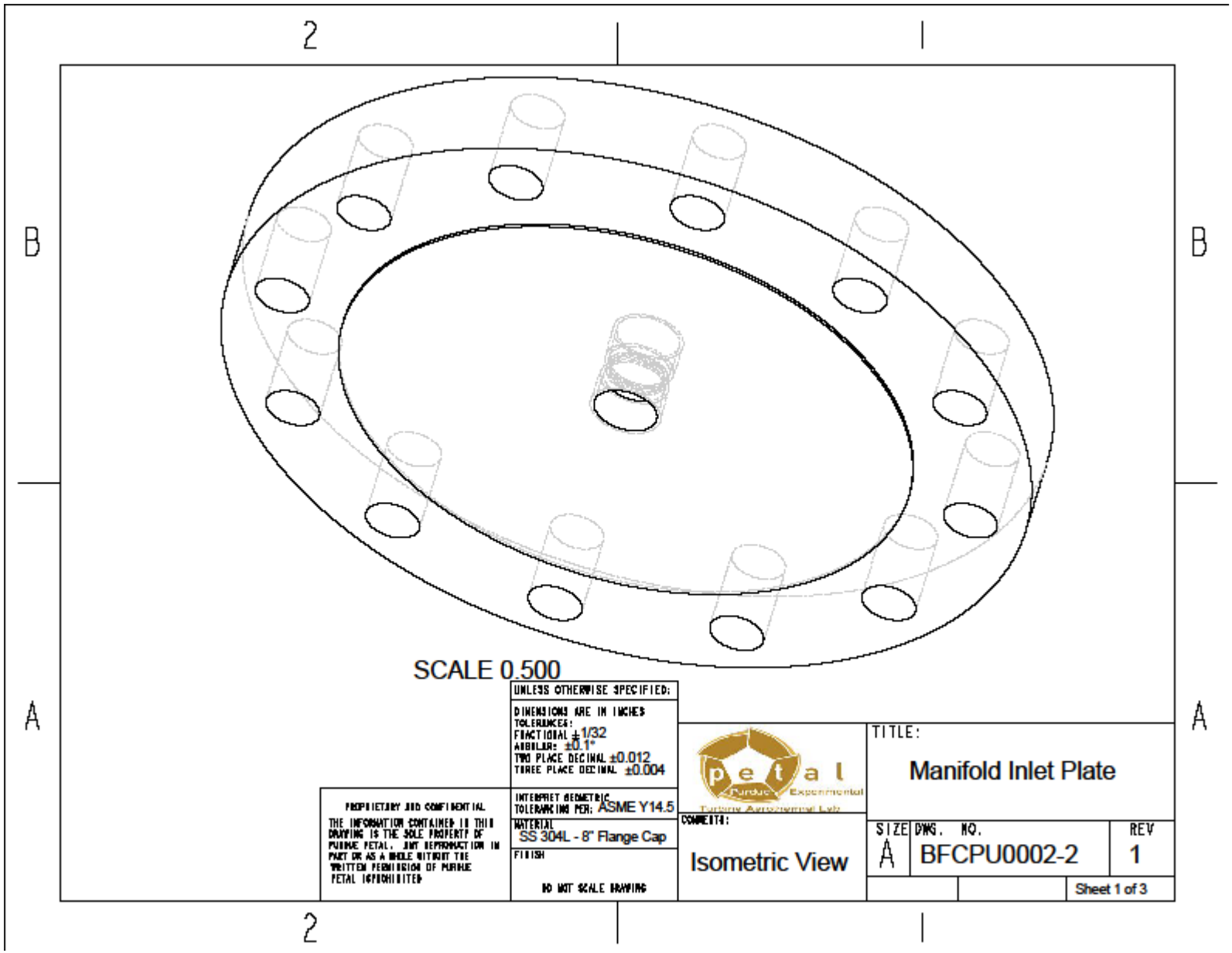

UNLESS OTHERWISE SPECIFIED:

DIMENSIONS ARE IN INCHES
TOLERANCES:
FRACTIONAL ±1/32
ANGULAR: ±0.1°
TWO PLACE DECIMAL ±0.012
THREE PLACE DECIMAL ±0.004

INTERPRET GEOMETRIC TOLERANCING PER: ASME Y14.5

MATERIAL: SS 304L - 8" Flange Cap

FINISH

DO NOT SCALE DRAWING

DRAWN:

Isometric View

TITLE:

Manifold Inlet Plate

SIZE	DWG. NO.	REV
A	BFCPU0002-2	1

Sheet 1 of 3

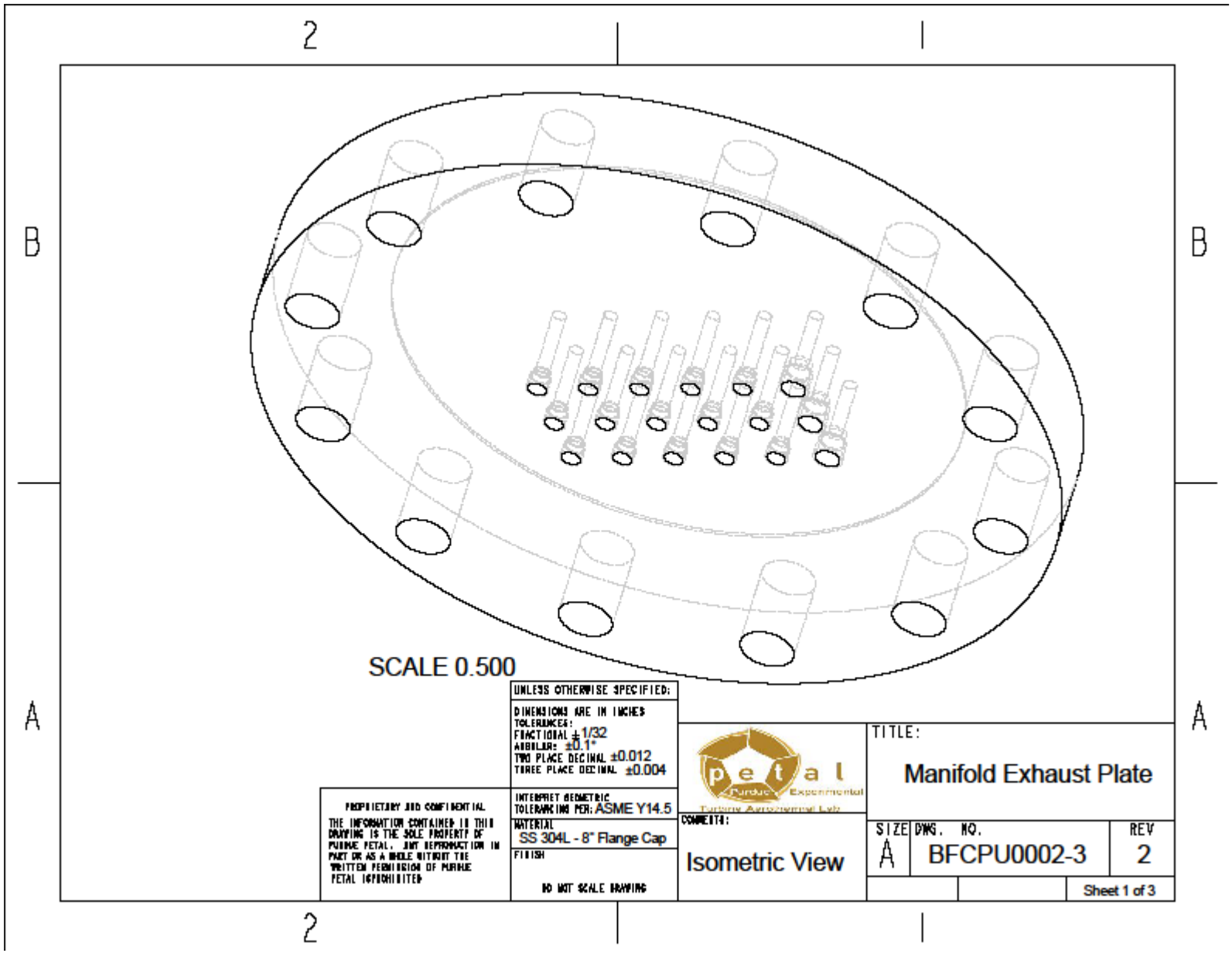
2
1
B
A
SCALE 0.500
UNLESS OTHERWISE SPECIFIED:
DIMENSIONS ARE IN INCHES
TOLERANCES:
FRACTIONAL ±1/32
ANGULAR: ±0.1°
TWO PLACE DECIMAL ±0.012
THREE PLACE DECIMAL ±0.004
INTERPRET GEOMETRIC TOLERANCING PER: ASME Y14.5
MATERIAL
SS 304L - 8" Flange Cap
FINISH
DO NOT SCALE DRAWING
PROPRIETARY AND CONFIDENTIAL
THE INFORMATION CONTAINED IN THIS DRAWING IS THE SOLE PROPERTY OF PURDUE PETAL. ANY REPRODUCTION IN PART OR AS A WHOLE WITHOUT THE WRITTEN PERMISSION OF PURDUE PETAL IS PROHIBITED
petal
Purdue Experimental
Future Aerospace Lab
COMMENTS:
Isometric View
TITLE:
Manifold Exhaust Plate
SIZE
A
DWG. NO.
BFCPU0002-3
REV
2
Sheet 1 of 3

APPENDIX B. TABLE OF EXPERIMENTAL CASE NAMES

Name	Re [1/m x10^6]	Mach [-]	PR [-]	f [Hz]
H-01-196	2.6	0.600	-	-
H-01-390	2.5	0.575	-	-
H-01-588	2.4	0.550	-	-
H-01-749	2.4	0.530	-	-
H-01-838	2.4	0.520	-	-
H-02-855	2.8	0.530	-	-
H-02-888	2.8	0.524	-	-
H-03-792	3.2	0.530	-	-
H-04-381	3.9	0.560	-	-
H-04-548	3.8	0.575	-	-
H-04-708	3.8	0.550	-	-
H-04-872	3.7	0.530	-	-
H-04-938	3.7	0.520	-	-
H-05-080	4.3	0.575	-	-
H-09-542	3.8	0.575	3.92	0
H-11-541	3.8	0.575	2.92	0
H-14-591	2.4	0.575	3.66	0
H-17-753	3.7	0.575	2.01	0
H-20-374	3.9	0.575	1.40	0
N-10-568	3.6	0.575	-	-
N-12-745	3.8	0.575	2.12	50
N-13-723	3.7	0.575	2.12	200
N-14-757	3.8	0.575	2.06	400
N-15-772	3.8	0.575	2.70	200
N-17-785	3.8	0.575	-	0
N-19-615	3.5	0.575	3.47	50
N-23-626	3.6	0.575	3.42	125
N-24-648	3.6	0.575	3.48	138
N-22-591	3.6	0.575	3.38	150
N-20-681	3.7	0.575	3.22	200
N-21-789	3.8	0.575	3.20	400

APPENDIX C. FUTURE WALL MEASUREMENTS

In addition to low frequency pressures that can be ascertained from pressure taps, 2 inserts were designed for the future use of high frequency wall measurement techniques. Two 1/4" through holes were added down stream of two flow injection ports. For the experiments conducted, blank dowels were used, so no high frequency wall measurements were obtained. For future works with the designed geometry there is the option of using devices such as wall-shear stress sensors and high frequency pressure sensors to obtain temporally resolved wall measurements.

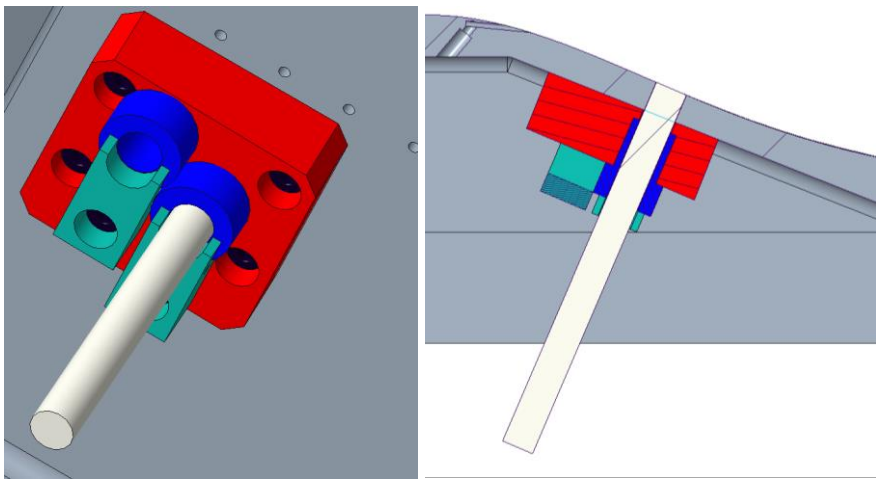

Figure 0.1. Sensor bracket for future surface quantity measurement technique

APPENDIX D. EXAMPLE OF UNCERTAINTY CALCULATION

This appendix contains an example of the calculation of uncertainty using CP as the derived quantity and Total inlet pressure as the measurement. It then shows how the relative uncertainty in a derived quantity is calculated using the results of the variation and sensitivity with respect to each measured quantity.

The derived quantity is calculated as

$$C_{p,mean} = \frac{P_{0,inlet,mean} - P_{s,local,mean}}{P_{0,inlet,mean} - P_{s,exit,mean}}$$

The relative uncertainty, with respect to the mean value of the measured quantity was calculated.

$$Uncertainty\ of\ P_0\ in\ \%\ mean = \frac{Absolute\ Uncertainty_{P0}}{P_{0,mean}}$$

For each measured quantity, the derived quantity was calculated using the sum of the mean and the absolute uncertainty.

$$C_{p,P0+absolute\ uncertainty} = \frac{P_{0,inlet,mean} + Absolute\ Uncertainty_{P0} - P_{s,local,mean}}{P_{0,inlet,mean} + Absolute\ Uncertainty_{P0} - P_{s,exit,mean}}$$

The variation with respect to the measured quantity was calculated as

$$Vairation\ of\ C_p\ with\ respect\ to\ P_0 = \frac{C_{p,P0+absolute\ uncertainty} - C_{p,mean}}{C_{p,mean}}$$

The sensitivity of the derived quantity was then calculated with respect to the measured quantity

$$Sensitivity\ of\ C_p\ with\ respect\ to\ P_0 = \frac{Vairation\ of\ C_p\ with\ respect\ to\ P_0}{Uncertainty\ of\ P_0\ in\ \%\ mean}$$

This is repeated for every measured quantity. For C_p, it was repeated for local static and exit static pressures.

The relative uncertainty in C_p (δ_{CP}) wass calculated as the root mean squar of the variation in C_p caused by the absolute uncertainty of each measured quantity ($VAR_{\text{measured quantity}}$).

$$\delta_{CP} = \sqrt{VAR_{P0,inlet}{}^2 + VAR_{PS,Local}{}^2 + VAR_{PS,Exit}{}^2}$$

The 95 percent confidence band is then calculated as:

$$95\%\ Band_{CP} = C_{p,mean} * \delta_{CP}$$

This process is repeated for every derived quantity. The formulation only changes the number of variables for which the variation and sensitivity is calculated, and as a result the number of terms in the root mean square.

REFERENCES

Celik et Al., 2008, “Procedure for Estimation and Reporting of Uncertainty Due to Discretization in CFD Applications,” Journal of Fluids Engineering, 130/078001-1-4.

Coull, J.D.; Hodson, H.P. “Unsteady boundary-layer transition in low-pressure turbines”. J. Fluid Mech. 2011, 681, 370–410.

FESTO. (2019). Solenoid valves, MHJ, fast-switching valves, NPT. Festo Corporation, Islandia, NY.

Greenblatt, D., & Wygnanski, I. J. (2000). The control of flow separation by periodic excitation. Progress in aerospace Sciences, 36(7), 487-545.

Iyer, P. S., & Malik, M. R. (2016). Wall--modeled Large Eddy Simulation of Flow Over a Wall--mounted Hump. In 46th AIAA Fluid Dynamics Conference (p. 3186).

Kandala, R., & Candler, G. V. (2004). Numerical studies of laser-induced energy deposition for supersonic flow control. AIAA journal, 42(11), 2266-2275.

Kiefer, N. (2022). Personal Communication.

Luedke, J., Graziosi, P., Kirtley, K., and Cerretelli, C., 2005, “Characterization of Steady Blowing for Flow Control in a Hump Diffuser,” AIAA journal, 43(8), pp. 1644-1652.

Martínez, D., Pescini, E., Marra, F., De Giorgi, M., and Ficarella, A., "Analysis of the Performance of Plasma Actuators Under Low-Pressure Turbine Conditions Based on Experiments and URANS Simulations," Proc. ASME Turbo Expo 2017: Turbomachinery Technical Conference and Exposition, American Society of Mechanical Engineers, pp. V02AT40A034-V002AT040A034.

Moffat, R. J. (1988). Describing the uncertainties in experimental results. Experimental thermal and fluid science, 1(1), 3-17.

Morgan, P. E., Rizzetta, D. P., & Visbal, M. R. (2007). Large-eddy simulation of separation control for flow over a wall-mounted hump. AIAA journal, 45(11), 2643-2660.

Opaits, D. F., Likhanskii, A. V., Neretti, G., Zaidi, S., Shneider, M. N., Miles, R. B., & Macheret, S. O. (2008). Experimental investigation of dielectric barrier discharge plasma actuators driven by repetitive high-voltage nanosecond pulses with dc or low frequency sinusoidal bias. Journal of Applied Physics, 104(4), 043304.

Pack, L. G., & Seifert, A. (1999). Periodic excitation for jet vectoring and enhanced spreading, AIAA Paper No. 99-0672. In 37th AIAA Aerospace Sciences Meeting, Reno, NV.

Pescini, E., Marra, F., De Giorgi, M., Francioso, L., and Ficarella, A., 2017, "Investigation of the boundary layer characteristics for assessing the DBD plasma actuator control of the separated flow at low Reynolds numbers," Experimental Thermal and Fluid Science, 81, pp. 482-498.

Praisner, T. J., Grover, E. A., Knezvici, D. C., Popovic, I., Sjolander, S. A., Clark, J. P., and Sondergaard, R., 2013, “Toward the Expansion of Low-Pressure-Turbine Airfoil Design Space,” ASME J. Turbomach., 135(6), p. 061007.

Saavedra, J. “Determining the dynamic scales of the boundary layer and flow separation inception: Analysis towards efficient flow control. Diss. Purdue University Graduate School, 2018.

Saavedra J., Paniagua G., 2021, “Experimental analysis of Reynolds effect on flow detachment and sudden flow release on a wall-mounted hump”. Experimental Thermal and Fluid Science. Vol. 126, paper 110398.

Schmitz, J. T., Perez, E., Morris, S. C., Corke, T. C., Clark, J. P., Koch, P. J., & Puterbaugh, S. L. (2016). Highly Loaded Low-Pressure Turbine: Design, Numerical, and Experimental Analysis. Journal of Propulsion and Power, 32(1), 142-152.

Seifert, A., and Pack, L. G., 2002, "Active flow separation control on wall-mounted hump at high Reynolds numbers," AIAA journal, 40(7), pp. 1363-1372.

Volino, R. J., 2003, ‘‘Passive Flow Control on Low-Pressure Turbine Airfoils,’’ ASME J. Turbomach., 125, pp. 754–764

You, D., Wang, M., & Moin, P. (2006). Large-eddy simulation of flow over a wall-mounted hump with separation control. AIAA journal, 44(11), 2571-2577.

PENDING PUBLICATION

Nowak, H. D., Lluesma-Rodriguez, F., Rahbari, I., Clark, J. P., and Paniagua, G., "Response of Separated Boundary Layers to Steady and Pulsated Flow Injection in Transonic Internal Flows," Proc. ASME Turbo Expo 202: Turbomachinery Technical Conference and Exposition, American Society of Mechanical Engineers, pp. Pending.